# 國 立 交 通 大 學

## 電機與控制工程學系

## 博 士 論 文

**具串連結構 CMOS-MEMS 靜電梳狀致動器之**

**實現**

**The Implementation of Cascade Electrostatic**

**CMOS-MEMS Comb-Drive Actuator**


博士生: 郭 秦 輔

指導教授: 邱 俊 誠　博士



中華民國 九十六 年 十 月

# 具串連結構 CMOS-MEMS 靜電梳狀致動器之實現

The Implementation of Cascade Electrostatic CMOS-MEMS Comb-Drive Actuator

研 究 生：郭秦輔 Student: Chin-Fu Kuo
指導教授：邱俊誠 博士 Advisor: Dr. Jin-Chern Chiou

國 立 交 通 大 學
電 機 與 控 制 工 程 學 系
博 士 論 文

**A Dissertation**

**Submitted to Department of Electrical and Control Engineering**

**College of Electrical Engineering and Computer Science**

**National Chiao Tung University**

**in Partial Fulfillment of the Requirements**

**for the Degree of**

**Doctor of Philosophy**

**in**

**Electrical and Control Engineering**

**October 2007**

**Hsinchu, Taiwan, Republic of China**

中華民國九十六年十月

# 具串連結構 CMOS-MEMS 靜電梳狀致動器之實現

學生：郭 秦 輔　　　　指導教授：邱 俊 誠

國立交通大學電機與控制工程學系

## 摘要

本論文提出具有串連結構的CMOS-MEMS靜電梳狀致動器(Cascade electrostatic comb-drive actuator)。由於靜電式梳狀致動器(Electrostatic comb-drive actuator)在致動時會發生側向不穩定(Side-instability)的現象，所以致動器的行距會受此一現象大大限制；本論文所提出一種新型的串連式靜電梳狀致動器，利用此串連結構不僅可以有效的增加靜電梳狀致動器的行距，而且與傳統的靜電梳狀致動器相比，此種串連結構在增加致動行距時，並不需要增加額外的驅動電壓。為了使致動器的各級驅動訊號可以達到良好的電性分離，此種串連式的靜電梳狀致動器必須具有多層結構的特性。因此，元件的製作必須結合標準CMOS製程與CMOS微加工後製程(Post-CMOS micromachining steps)，經由此一整合性的製程，致動器會具有多層結構的特性，使各級驅動訊號將可達到良好的分離，並可使致動器具有垂直致動的能力。實驗結果顯示，水平式的串連靜電梳狀致動器(Lateral cascade electrostatic comb-drive actuator)可以增加 200% 的致動行距，而垂直式的串連靜電梳狀致動器(Vertical cascade electrostatic comb-drive actuator)可以增加 188% 的致動行距。實驗結果證明，此種串連式結構的設計確實具有非常好的能力能將致動器的致動行距增大。

# THE IMPLEMENTATION OF CASCADE ELECTROSTATIC CMOS-MEMS COMB-DRIVE ACTUATOR

Chin-Fu, Kuo (Department of Electrical and Control Engineering)
Dissertation directed by Professor Jin-Chern, Chiou

## ABSTRACT

Electrostatic comb-drive actuators have been developed and employed for many applications. However, side instability (side pull-in) limits the actuator stroke constraining its applications. Hence, extending actuation stroke is an important issue for designing electrostatic comb-drive actuators. In this dissertation, two cascade electrostatic comb-drive actuators, namely cascade lateral electrostatic comb-drive actuator and cascade vertical electrostatic comb-drive actuator are developed for improving the stroke of electrostatic comb-drive actuators. With the cascade configuration, the actuation stroke can be improved greatly. To implement the cascade electrostatic comb-drive actuators, the Taiwan Semiconductor Manufacturing Company (TSMC) 0.35 μm two polysilicon layers and four metal layers (2p4m) complementary metal-oxide-semiconductor (CMOS) and post-CMOS micromachining steps are employed to fabricate the device. Due to the multilayer characteristic of the microstructure, the electric signal isolation and vertical motion can be achieved. Experimental results indicated that the stroke of the lateral and vertical cascade electrostatic comb-drive actuators can be improved 200% and 188% respectively without adding extra driving voltage. These results demonstrated that the proposed cascade configurations have the capability to improve the actuation stroke of electrostatic actuators.

# 誌　謝

感謝我的指導教授 邱俊誠博士，於博士班求學階段於學術上的指導與待人處事方面的諄諄教誨，師恩浩蕩，學生永銘於心。

感謝我碩士班指導教授，義守大學電機系 孫永莒教授，開創了我的學術視野，激勵出我攻讀博士班的原動力。

感謝國家晶片中心(CIC)所提供的製程服務，讓元件的製作能順利完成，完成整個論文，特此鳴謝。

感謝我的博士學位口試委員：清大動機系 方維倫教授（召集人）、國家晶片中心副主任 邱進峰博士、交大電工系 黃遠東教授、交大機械系 徐文祥教授、交大電控系 邱一教授對於我博士論文的細心建議與指導，使得學生的論文更加趨於完善，讓學生獲益良多，特此鳴謝。

感謝國家晶片中心(CIC)的賴建銘先生，在量測方面多方面的協助我，使我在研究上能夠更加的完整，特此鳴謝。

感謝交大電控系96年度的研究所委員會的各位委員、博士班行政助理林滿足小姐與其他的行政助理，在我提出博士論文口試時給予的協助與建議，特此鳴謝。

感謝我的學長 林永峻博士，對於我的研究與生活上的種種協助與鼓勵，在未來的人生中，大家還可以共同努力、勉勵與提攜。也感謝這幾年博士班生活中有緣相遇到的博士班學弟們、碩士班學弟妹們、邱一老師碩士班學弟、還有行政助理楊可筠小姐、詹巧雯小姐，有各位的相伴與協助，使我的生活更加的多采多姿。

感謝小志，我的女友，這幾年默默的陪伴著我，因為她的陪伴，滋潤及豐富了我的研究生生涯，無時無刻的體諒與關懷，也消除了我許多的壓力與煩惱，這段日子的點點滴滴，都將會是畢生難忘的美好回憶。

最後，僅以此論文獻給我的父母親，感謝他們這麼多年來不斷的支持與鼓勵，讓我的求學生涯無後顧之憂，可以順利完成博士學位，成功的邁向人生另一階段，謝謝你們。

# CONTENT

摘要 ........ i

Abstract ........ ii

誌　謝 ........ iii

Content ........ iv

List of Figure ........ vi

List of Table ........ ix

Chapter I ........ 1

INTRODUCTION ........ 1

1.1 Micro-Electro-Mechanical Systems (MEMS) ........ 1
1.2 MEMS Fabrication ........ 3
1.2.1 Surface Micromachining Process ........ 4
1.2.2 Buck Micromachining Process ........ 7
1.2.3 High Aspect Ratio Process ........ 9
1.3 Review of Micro-Actuator in MEMS ........ 10
1.4 Dissertation Work ........ 12

Chapter II ........ 13

CMOS-MEMS FABRICATION PROCESS ........ 13

2.1 Introduction ........ 13
2.2 CMOS MEMS ........ 13
2.2.1 Pre-CMOS ........ 14
2.2.1 Intra-CMOS ........ 15
2.2.1 Post-CMOS ........ 17
2.3 Fabrication Processes ........ 19
2.3.1 CMOS Fabrication Process ........ 19
2.3.2 Post-CMOS Micromachining Step of CIC ........ 22

Chapter III ........ 25

CASCADE LATERAL ELECTROSTATIC COMB- DRIVE ACTUATOR ........ 25

3.1 Introduction ........ 25
3.2 Side Instability of Lateral Electrostatic Comb-Drive Actuators ........ 25
3.3 Design of The Cascade Lateral Electrostatic Comb-Drive Actuator ........ 32

3.3.1 Design concept........................................32
3.3.2 FEM Simulations........................................33
3.3.3 Electric Isolation........................................35
3.4 Experimental Results........................................36
3.5 Remark Conclusion........................................40
Chapter IV........................................41
CASCADE VERTICAL ELECTROSTATIC COMB- DRIVE ACTUATOR........................................41
4.1 Introduction........................................41
4.2 Side Instability of Vertical Electrostatic Comb-Drive Actuator........................................41
4.3 Design Concept and FEM Simulation........................................44
4.3.1 Design concept and FEM Simulation........................................44
4.3.2 Actuation Principle........................................46
4.4 Experiment Results........................................47
4.5 Remark Conclusion........................................48
Chapter V........................................50
CONCLUSIONS........................................50
5.1 Summary of This Dissertation........................................50
5.2 Contributions........................................50
5.3 Suggestions for Future Research........................................51
Appendix A: CMOS Process Flow........................................53
Bibliography........................................60
Biography........................................68
Publication........................................69

E S A 1896

# LIST OF FIGURE

Fig. 1.1 ADXL50: The first surface micromachined accelerometer product introduced by Analog Devices©[2] ..... 1

Fig. 1.2 Ink jet head introduced by SEIKO EPSON© [3] ..... 2

Fig. 1.3 DMD (Digital Micro-mirror Device) introduced by TI©[4] ..... 2

Fig. 1.4 The basic process flow of surface micromachining ..... 5

Fig. 1.5 Cross sectional view showing all 7 layers of the PolyMUMPs process (not to scale) ..... 6

Fig. 1.6 SEM images of a micromirror fabricated through PolyMUMPs with (a) micromirror device (b) mirror and springs (c) pre-stress comb actuator. ..... 7

Fig. 1.7 Schematic view of various structures manufacturing by bulk micromachining [12] ..... 8

Fig. 1.8 Difference between (a) anisotropic and (b) isotropic wet etching ..... 9

Fig. 1.9 Schematic process flow of LIGA [21] ..... 10

Fig. 2.1 Schematic cross-sectional views of two pre-CMOS MEMS processes: (a) $M^3$EMS technology developed by Sandia National Laboratories [47]. (b) SOI MEMS with 10 μm device layer for fabrication of single-crystalline silicon inertial sensors [52]. ..... 15

Fig. 2.2 Schmatic cross-sectional view of two intra-CMOS processes: (a) Analog Devices' integrated MEMS technology with an n+-diffusion interconnect structure between polysilicon microstructure and on-chip electronics [58].(b) Srface micromachined pressure sensor element developed at Toyota Central R&D Laboratories [59]. ..... 17

Fig. 2.3 Schematic cross-sections of (a) polysilicon and (b) polycrystalline silicon germanium (poly-SiGe) microstructures fabricated by post-CMOS surface

micromachining techniques on top of a completed CMOS substrate wafer [75,76]......................................................................................................19
Fig. 2.4 Thickness of each layer for the TSMC CMOS process...........................22
Fig. 2.5 Post-CMOS micromachining steps: (a) cross-sectional view of MEMS devices after completing TSMC 0.35μm 2P4M fabrication processes, (b) patterning of PR mask to protect unneeded etched regions, (c) performing anisotropic RIE to etch silicon dioxide, (d) cross-sectional view of device after completing post-CMOS micromachining steps..................................24
Fig. 3.1 Schematic drawing of a conventional electrostatic comb-drive actuator. 26
Fig. 3.2 Schematic drawings of an electrostatic comb-drive actuator (a) before actuation, (b) stable actuation condition, (c) side instability actuation condition. ......................................................................................................27
Fig. 3.3 Relationship between $K_e$, $K_x$, and $K_y$......................................................30
Fig. 3.4 Schematic drawings of (a) an electrostatic comb-drive actuator with tilted suspended springs, (b) an electrostatic comb-drive actuator with pre-bent suspended springs and linearly engaging comb fingers, (c) an electrostatic comb-drive actuator with two sets of comb electrodes...............................31
Fig. 3.5 Schematic drawings of an electrostatic comb-drive actuator with three actuation stages. ..........................................................................................33
Fig. 3.6 3D model of the electrostatic comb-drive actuator with one stage. .........34
Fig. 3.7 3D model of the electrostatic comb-drive actuator with three stages. .....34
Fig. 3.8 FEM simulation results of an electrostatic comb-drive actuator with 100V driving voltage. ..........................................................................................34
Fig. 3.9 FEM simulation results of a cascade electrostatic comb-drive actuator with 100V driving voltage. ..........................................................................35
Fig. 3.10 Schematic Cross-section of movable comb finger structure, fixed comb

finger structure, and connection frame. ....................................................36
Fig. 3.11 The SEM image of the fabricated device (a) top view, (b) 45° view. ...37
Fig. 3.12 The image of the optical interferometric profiler. ................................38
Fig. 3.13 The static characteristic of the design cascade electrostatic comb-drive actuator device. The solid line represents the simulation results of 1st stage, and the dash lines represent measured data of three different stage. ............39
Fig. 3.14 The displacement versus driving voltage by driving three stages simultaneously. The solid line corresponds to simulation results, and dotted line corresponds to measured data. ...........................................................39
Fig. 4.1 Schematic drawing of comb fingers (a) not engaged, (b) partially engaged, and fully engaged. ........................................................................42
Fig. 4.2 Cross-sectional view of side pull-in condition. ...................................43
Fig. 4.3 Schematic drawing of CVCA with four stages. ......................................45
Fig. 4.4 FEM simulation results of simplified CVCA model (a) without driving voltage and (b) with driving voltage. ..........................................................45
Fig. 4.5 Cross-sectional view of fixed comb fingers and movable fingers. ..........46
Fig. 4.6 SEM image of fabricated device. ..........................................................47
Fig. 4.7 Static characteristic of fabricated device. ...............................................48

# LIST OF TABLE

Table 1.1: Thickness of each layer in PolyMUMPs process. ..................................6

Table 3.1: The Parameter Table of FEM Simulation .............................................35

# CHAPTER I

# INTRODUCTION

## 1.1 Micro-Electro-Mechanical Systems (MEMS)

For the last twenty years, engineers have made a lot of effort on delivering micro-devices for practical applications including automotive safety, military industry, telecommunication, human health-care, biochemical analysis, and consumer electronics [1]. These devices including accelerometer (Fig. 1.1)[2], inkjet print head (Fig. 1.2) [3], and digital micro-mirror device (Fig. 1.3)[4] that are successfully commercialized through MEMS fabrication techniques. The accelerometer embedded in the airbag system is utilized to protect passengers from vehicle accident. The development of array of inkjet nozzles brings the high quality printings while digital micro-mirror evolutes the display technologies.

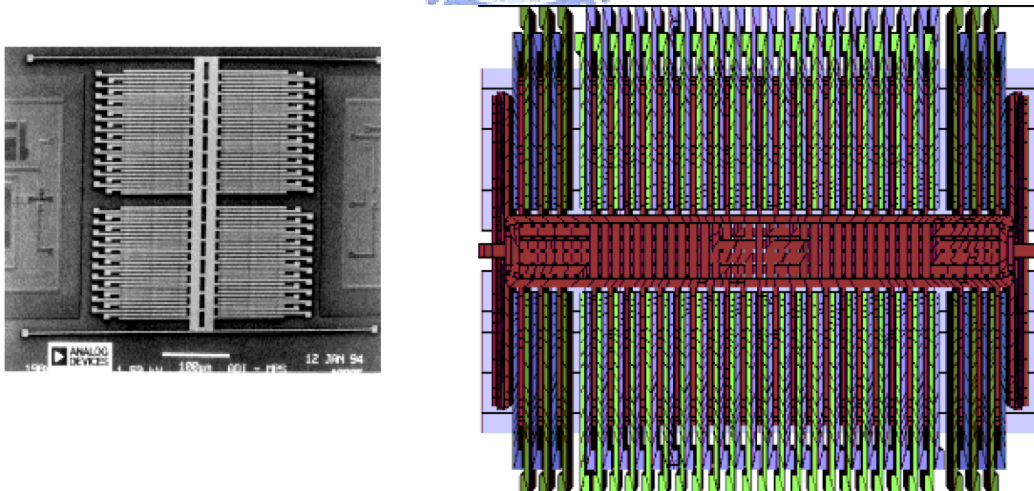


Fig. 1.1 ADXL50: The first surface micromachined accelerometer product introduced by Analog Devices©[2]

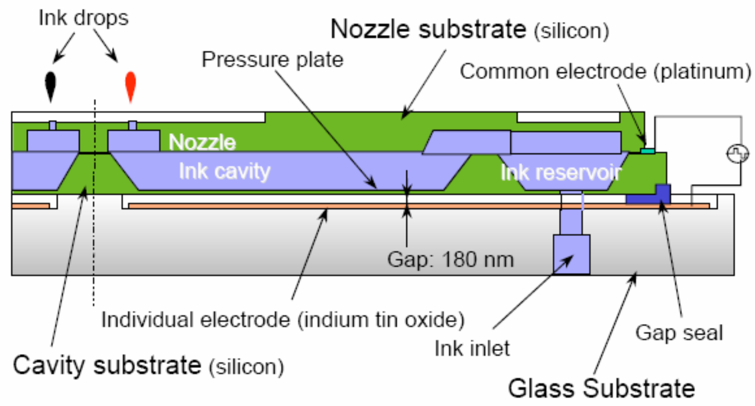


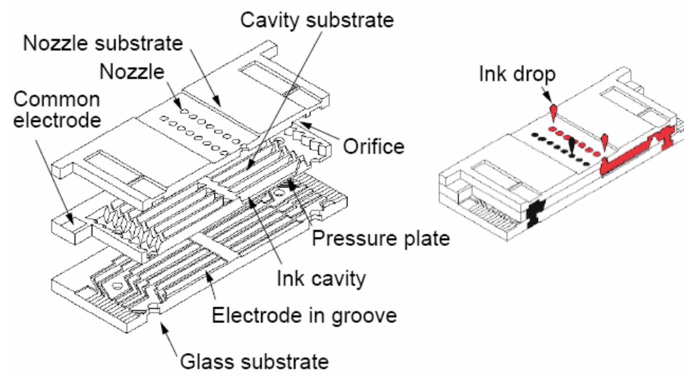


Fig. 1.2 Ink jet head introduced by SEIKO EPSON© [3]

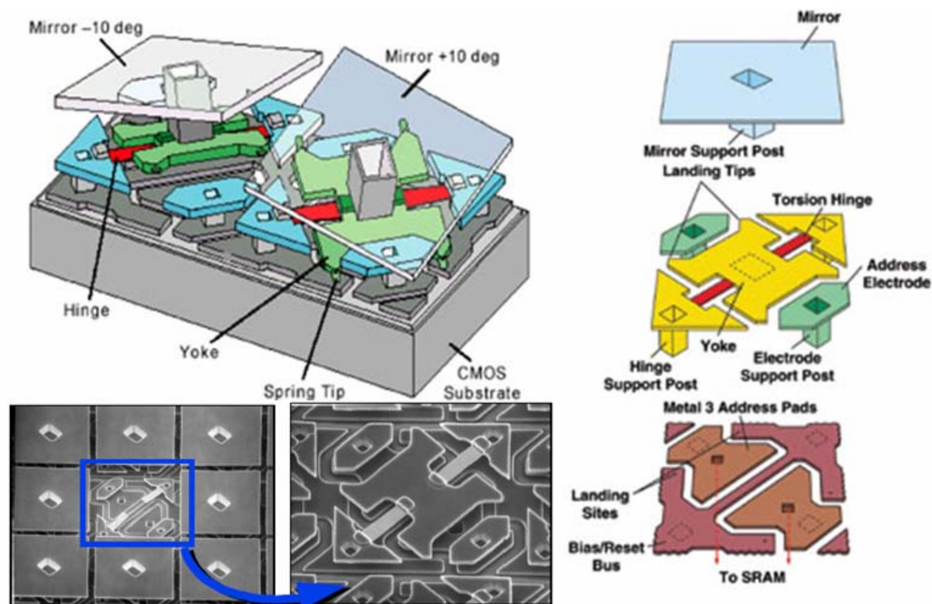


Fig. 1.3 DMD (Digital Micro-mirror Device) introduced by TI©[4]

Note that, Micro-Electro-Mechanical Systems (MEMS) enable suspended microstructures to be moved precisely and integrated with microelectronic circuits monolithically on a chip to perform or provide analog tuning or digital switching of linear or angular motion [5]. It has been recognized as one of the most promising technologies for the 21st Century and has the potential to revolutionize industrial and consumer products by combining microelectronics with micromachining technology. Furthermore, by merging the functions of sensing and actuation with communication and computation, the integrated micro-systems are created to have smart functions that have the potential to dramatically affect of all of our lives and the way we live [6].

## 1.2 MEMS Fabrication

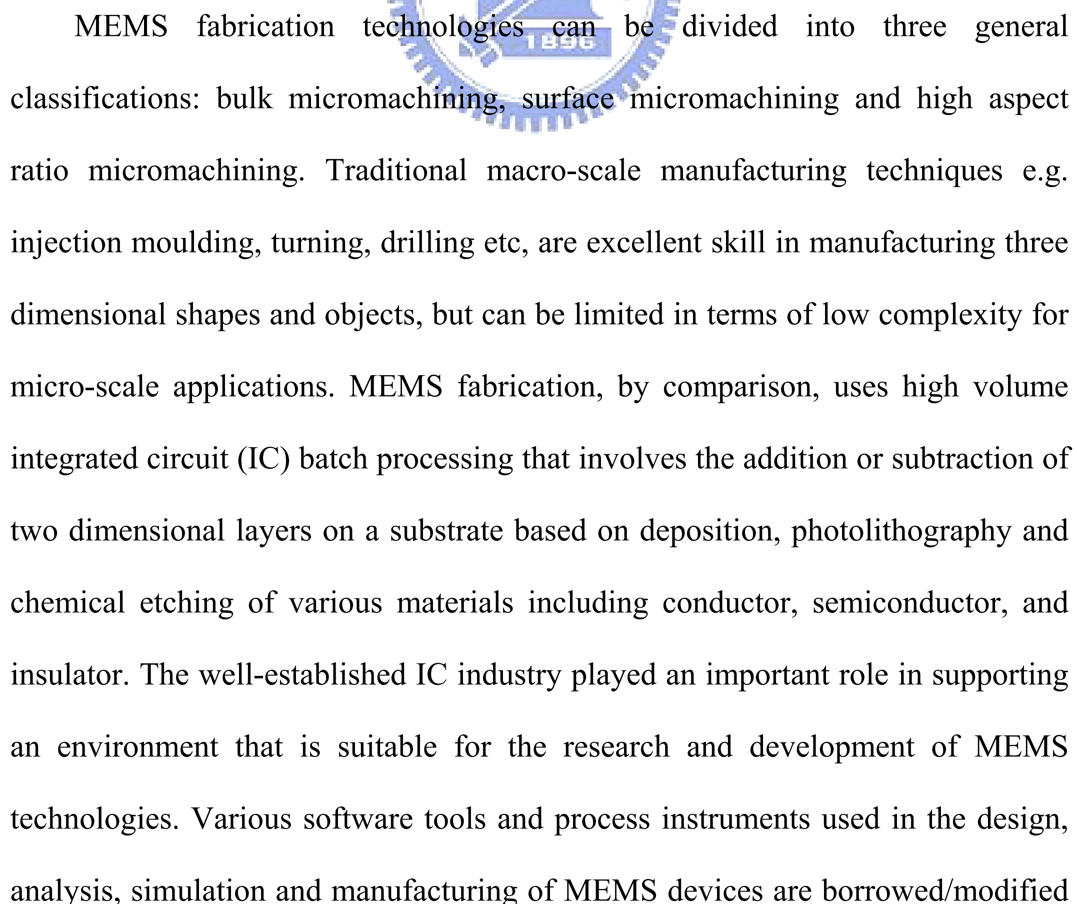

MEMS fabrication technologies can be divided into three general classifications: bulk micromachining, surface micromachining and high aspect ratio micromachining. Traditional macro-scale manufacturing techniques e.g. injection moulding, turning, drilling etc, are excellent skill in manufacturing three dimensional shapes and objects, but can be limited in terms of low complexity for micro-scale applications. MEMS fabrication, by comparison, uses high volume integrated circuit (IC) batch processing that involves the addition or subtraction of two dimensional layers on a substrate based on deposition, photolithography and chemical etching of various materials including conductor, semiconductor, and insulator. The well-established IC industry played an important role in supporting an environment that is suitable for the research and development of MEMS technologies. Various software tools and process instruments used in the design, analysis, simulation and manufacturing of MEMS devices are borrowed/modified

from the IC technology. Accordingly, the 3D MEMS structure is established from patterning and interaction of the 2D layers. Additional layers can be added using a variety of thin-film and bonding techniques as well as by etching through sacrificial ‘spacer layers’ [7]. Here, we introduce these techniques as well as provide design issues in practical applications.

### 1.2.1 SURFACE MICROMACHINING PROCESS

Different to bulk micromachining, surface micromachining does not remove material from the bulk silicon substrate, instead surface micromachining constructs structures on the surface of the silicon substrate by adding thin/thick films. Scientists at Westinghouse Electric Corp., and IBM Corp. had been demonstrated the potential of fabricating MEMS devices using surface micromachining in the 1960s and 1970s [8,9]. In surface micromachining, material is added on the substrate in the form of layers of thin films. These thin films can be characterized as structural layers or sacrificial layers. A structural layer is a material out of which the free-standing structure is made (generally polysilicon, silicon nitride and aluminium) and a sacrificial material, deposited wherever either an open area or a free-standing mechanical structure is required (usually an oxide). These layers are deposited and subsequently etched in sequence, with the sacrificial material being finally wet etched away to release the final structure. Each additional layer is accompanied by an increasing level of complexity and a resulting difficulty in fabrication [7]. Fig. 1.4 shows a basic process steps in surface micromachining [10].

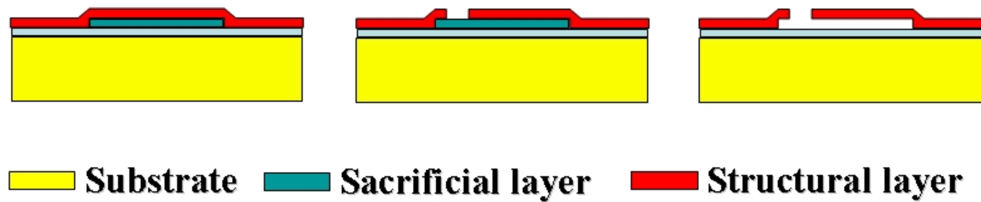


Fig. 1.4 The basic process flow of surface micromachining

A well known surface micromachining process is the Cronos/MEMSCAP PolyMUMPs process. The Multi-User MEMS Process (MUMPs) was developed at Berkeley Sensors and Actuators Center (BSAC) of University of California in the late 80's and early90's. In the past few days, MEMSCAP offers three standard processes as part of the MUMPs® program: PolyMUMPs, a three-layer polysilicon surface micromachining process; MetalMUMPS, an electroplated nickel process; and SOIMUMPs, a silicon-on-insulator micromachining process. They are commercial program that provides cost-effective, proof-of-concept MEMS fabrication to industry, universities, and government worldwide. As a result, the MEMS engineers/researchers can share their design space for cost-efficient research and development as well as accelerate the schedule of mass production.

The PolyMUMPs process itself consists of a non-patternable nitride isolation layer, three polysilicon layers (one polysilicon ground layer (plane layer) and two structural polysilicon layers), two oxide release layers, and one metal layer for electrical connection and reflectivity enhancement. Polysilicon is used as the structural material, deposited oxide (PSG) as the sacrificial material, and silicon nitride for electrical isolation from the substrate. Figure 1.5 shows the cross-sectional view of the PolyMUMPs process. The thickness of each layer is listed in the table 1.1. Figure 1.6 shows scanning electron microscope (SEM)

images of the micromirror fabricated through PolyMUMPs process. This micromirror is actuated by two pre-stress comb-drive actuators (PCA); hence, the micromirror can achieve rotation and vertical motion.

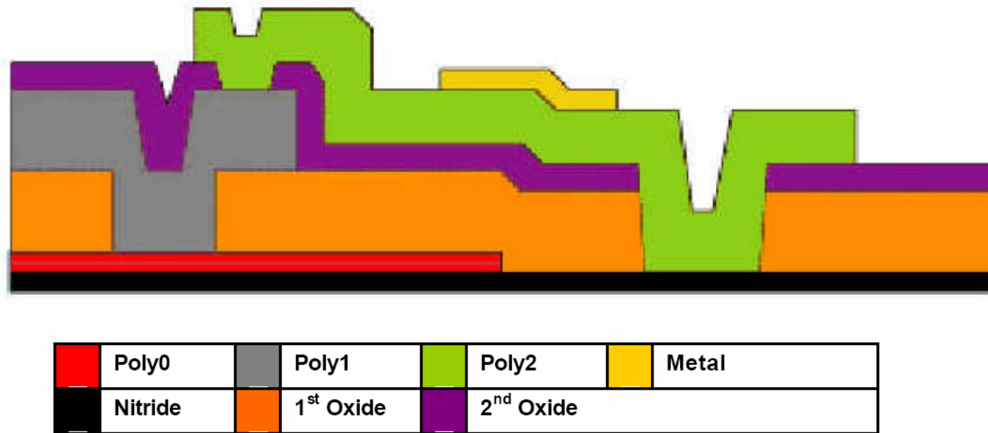


Fig. 1.5 Cross sectional view showing all 7 layers of the PolyMUMPs process (not to scale).

TABLE 1.1: THICKNESS OF EACH LAYER IN POLYMUMPS PROCESS.

| Layer | Thickness (μm) |
|---|---|
| Metal (Au) | 0.5 |
| Poly2 | 1.5 |
| 2nd Oxide | 0.75 |
| Poly1 | 2.0 |
| 1st Oxide | 2.0 |
| Poly0 | 0.5 |
| Nitride | 0.6 |

In addition, dissolving the sacrificial layer to free the structural elements, known as release process, plays a key step in the surface micromachining. Stiction, adhesion of suspended structures and the other surfaces, is the main post process setback existed in the surface micromachining. It has been widely reported to be

responsible for greatly curtailing the yield and reliability of the fabricated MEMS devices due to the phenomenon of stiction. There are several terms to evolved stiction problem such as adhesion due to Van Der Waals force, electrostatic force, capillary force and contamination [11]. A commercialized $CO_2$ super critical drying machine will be used to improve the stiction problem in surface micromachining.

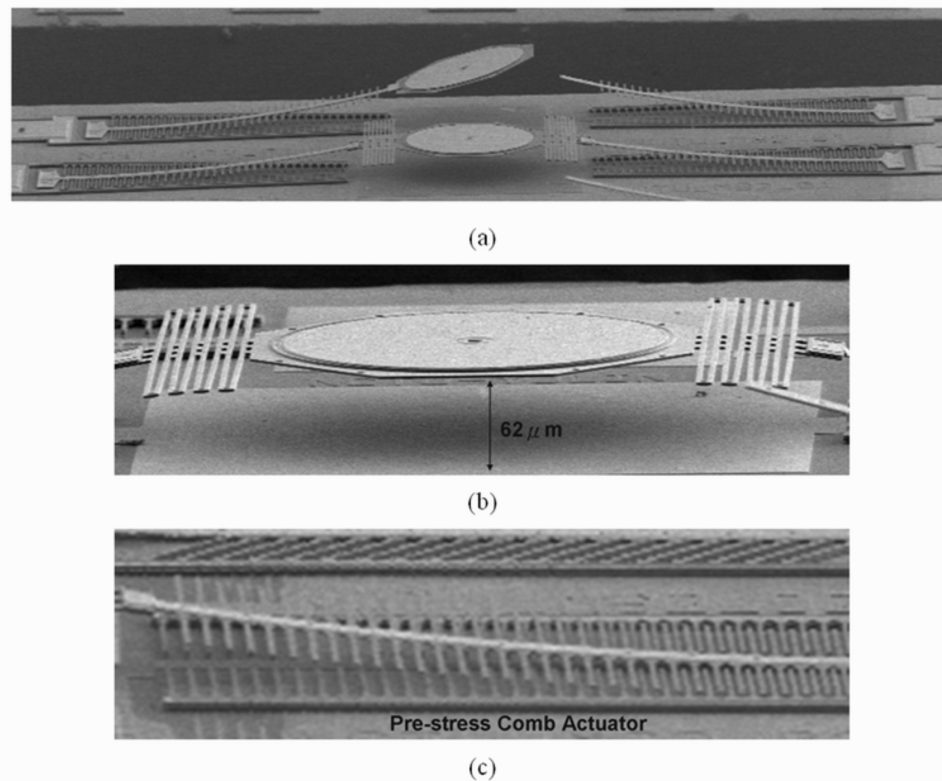


Fig. 1.6 SEM images of a micromirror fabricated through PolyMUMPs with (a) micromirror device (b) mirror and springs (c) pre-stress comb actuator.

### 1.2.2 BUCK MICROMACHINING PROCESS

The bulk micromachining technique is one of the most popular micromachining techniques. In bulk micromachining, the 3D mechanical structures such as cantilever beam, bridge, membrane, cavity, nozzle and trench

are formed by selectively removing (‘etching’) wafer material, as illustrated in Fig. 1.7 [12].

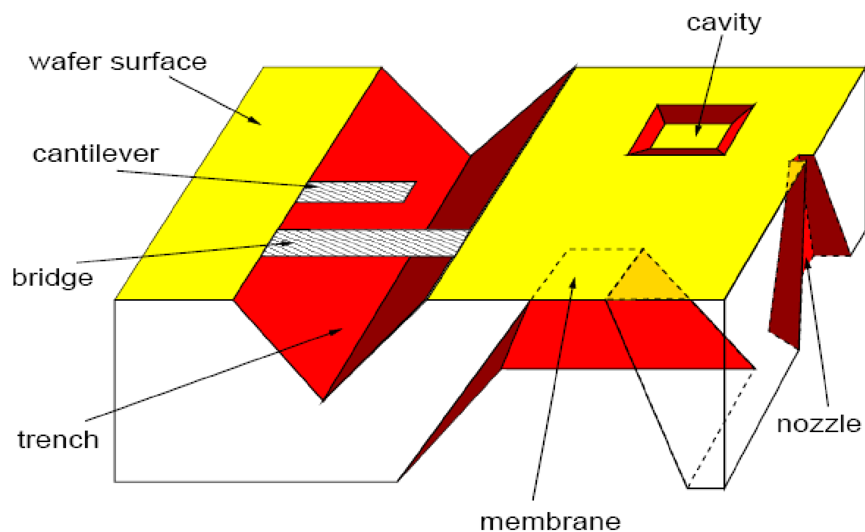


Fig. 1.7 Schematic view of various structures manufacturing by bulk micromachining [12].

In general, the process of bulk micromachining can be classified into isotropic and anisotropic etching. In isotropic etching, the etching rate is symmetrical in each crystalline orientation of silicon. Nevertheless, in anisotropic etching, the silicon substrate is etched with different rates along the different crystal plane, as shown in Fig. 1.8 Anisotropic etching techniques provide a high-resolution etching and tight dimensional control due to their high selectivity to different silicon crystallographic orientation [13,14].

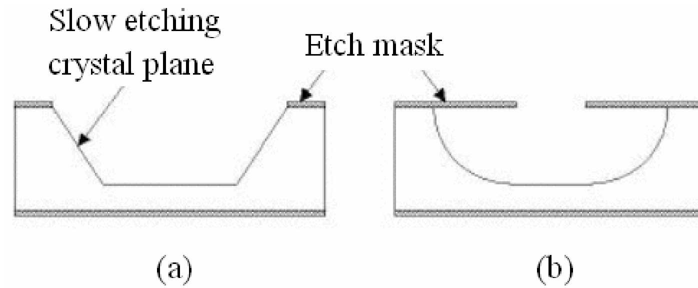


Fig. 1.8 Difference between (a) anisotropic and (b) isotropic wet etching

### 1.2.3 HIGH ASPECT RATIO PROCESS

The main high-aspect-ratio process in MEMS technologies including deep reactive ion etching (RIE) [15,16], LIGA [17,18], and electroplating [19,20] processes. Deep RIE is used to etch deep cavities in substrates with relatively high aspect ratio. Most systems utilize the so-called "Bosch process", in which a fluor polymer is used to passivate the etching of the sidewalls. Typical aspect ratios of 10 to 20 can be achieved. LIGA is an important tooling and replication method for high-aspect-ratio microstructures. The technique employs X-ray synchrotron radiation to expose thick acrylic resist of PMMA under a lithographic mask. The exposed areas are chemically dissolved and, in areas where the material is removed, metal is electroformed, thereby defining the tool insert for the succeeding moulding step. LIGA is capable of creating very finely defined microstructures up to 1000 μm high. Nevertheless, it is limited by the need to have access to an X-ray synchrotron facility. Fig. 1.9 shows the process flow of LIGA [21].

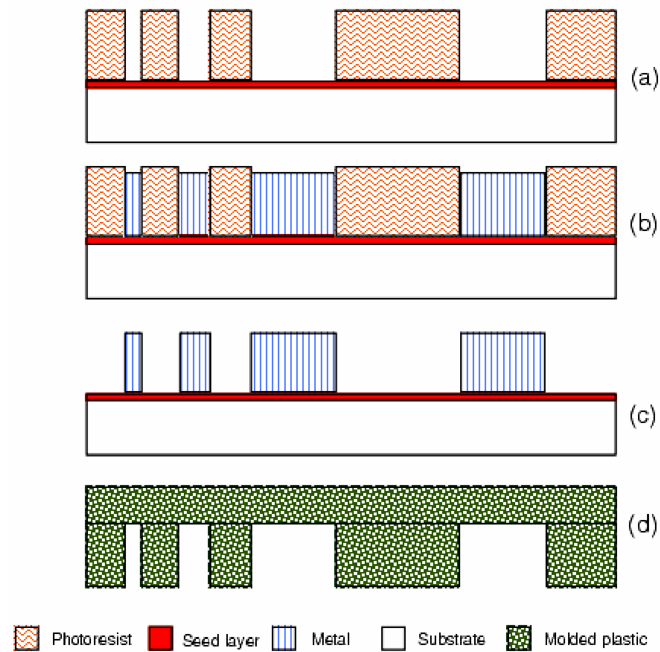


Fig. 1.9 Schematic process flow of LIGA [21]

## 1.3 REVIEW OF MICRO-ACTUATOR IN MEMS

Various actuation mechanisms, such as thermal/bimetallic bimorph [1,22,23], electromagnetic [24,25], piezoelectric [26,27] and electrostatic actuation [28,29], have been established and applied fundamentally in MEMS-based devices where mechanical actuation is required. In MEMS research, the most widely used micro-actuator is the electrostatic actuator [30]. The main benefit of the electrostatic actuator is its characteristic in small power consumption and fast response. The simplest electrostatic actuator is a parallel-plate electrostatic actuator. Such actuators have been utilized in many applications such as accelerometers [8,9,14], deformable optics [9], and relays [11]. However, parallel-plate electrostatic actuators suffer from pull-in phenomenon, which greatly constrains the stable traveling range of actuators (usually one-third of initial gap) [31]. To avoid the pull-in phenomenon, electrostatic comb-drive

actuators have been developed [32]. This actuator consists of two interdigitated finger structures with one fixed and the other connected to suspended springs, as shown in figure 1 (a). By applying a driving voltage between the movable comb fingers and fixed comb fingers, a displacement of movable comb fingers toward fixed comb fingers generates by the attractive electrostatic force. An electrostatic comb-drive actuator offers a near constant force over a large range of displacements. This actuator becomes a preferred design for implementing of electrostatic actuator. Applications of electrostatic comb-drive actuators include resonators [33,34], microgrippers [35], x-y microstages [36] and electromechanical filters [37].

Although electrostatic comb-drive actuators have these advantageous characteristics, the stable traveling range of the comb-drive actuator is limited by the electromechanical side instability (side pull-in). Side instability means that the situations in which the movable comb fingers move perpendicular to the stroke direction and then make contact with the fixed comb fingers. As the overlapping comb fingers area increasing with the forward displacement of the actuator, the cross-axis force become larger and larger that causes the fingers suddenly snapping over sideway. The side instability and stable traveling range of electrostatic comb-drive actuators depend on finger gap spacing, initial finger overlapping, and spring stiffness of suspended springs. Increasing finger gap spacing of an electrostatic comb-drive actuator is the simplest method for increasing the stable traveling range; nevertheless, this method results in a high driving voltage which is undesirable in numerous applications. To extend the stable traveling range of electrostatic comb-drive actuators, several approaches have been developed [38-41]. Among these methodologies, the most widely used method is to design different types of suspended springs to enhance the cross-axis

stiffness which need extra driving voltage to extend the traveling range.

## 1.4 DISSERTATION WORK

In this dissertation, we focus our research to develop cascade electrostatic comb-drive actuators. With the novel cascade multi-stage configuration, the traveling range can be extended without extra driving voltage..

The dissertation is organized as follows. Chapter 2 illustrates the fabrication processes including CMOS fabrication processes and post-CMOS micromachining steps. In chapter 3, a lateral cascade electrostatic comb-drive actuator is presented. The FEM simulation and experimental results are also given to demonstrate our design concept. Chapter 4 proposed a vertical type of the cascade electrostatic comb-drive different from the chapter 2, and the design concept, simulation, and experimental results are also given. Chapter 5 summarizes the accomplishments of the dissertation and provides suggestions for further research.

# CHAPTER II

# CMOS-MEMS FABRICATION PROCESS

---

## 2.1 INTRODUCTION

In this dissertation, the cascade micro-actuators were initially fabricated by the Taiwan Semiconductor Manufacturing Company (TSMC) 0.35 μm two polysilicon and four metal layers (2p4m) complementary metal-oxide-semiconductor (CMOS) fabrication processes. After CMOS process, post-CMOS micromachining steps are employed to define MEMS structures and release suspended structures. Section 2.2 gives an overview of the CMOS MEMS processes. CMOS processes and Post-CMOS micromachining steps are described in the section 2.3.

## 2.2 CMOS MEMS

While MEMS technology has made a substantial impact over the past decade at the device or component level, it has yet to realize the “S” in its acronym, as complex micro*systems* consisting of sensors and actuators integrated with sense, control, and signal-processing electronics are still beyond the current state of the art [42-46]. There are several incentives to co-fabricate MEMS devices and electronics on a single silicon chip, which apply to applications such as inertial sensors. The parasitic resistance and capacitance associated with the interconnection between the MEMS devices and electronics degrade electrical signal quality and hence degrade system performance. This problem is critical for

thin-film, surface micromachined devices in which changes in position are sensed as a small, capacitively induced current. If the MEMS devices can be co-fabricated with electronics on a single chip, the parasitic resistance and capacitance of these components can be greatly reduced. The elimination of chip-to-chip interconnections can also lead to more reliable packages. This is especially important for large arrays of MEMS devices that require independent addressing of each element, such as the micromirrors in an optical cross-connect switch, for which the monolithic integration of switching electronics can reduce the number of off-chip connections by orders of magnitude. Depending on the integration strategy that is adopted, the co-fabrication of microstructures and electronics on the same substrate may provide significant overall cost savings.

The integration of micromachining steps with CMOS process can be accomplished in different ways. The additional steps (or process modules) can either precede the CMOS process (pre-CMOS) or be preformed in between the CMOS process (intra-CMOS) or after the completion of the CMOS process (post-CMOS).

### 2.2.1 PRE-CMOS

In the pre-CMOS approach, the MEMS structures or part of them are formed before the regular CMOS process sequence. Pre-CMOS micromachining or 'MEMS-first' fabrication approaches avoid thermal budget constraints during the MEMS fabrication. In this way, e.g. thick polysilicon microstructures requiring stress relief anneals at temperatures up to 1100 ºC can be co-integrated with CMOS circuitry. Typically, the MEMS structures are buried and sealed during the initial process module. After the wafer surface is planarized, the preprocessed

wafers with embedded MEMS structures are used as starting material for the subsequent CMOS process. Challenges include the surface planarization required for the subsequent CMOS process and the interconnections between MEMS and circuitry areas. A number of pre-CMOS technologies have been developed [47-54]. Fig. 2.1 shows two schematic cross-sectional views of pre-CMOS MEMS processes.

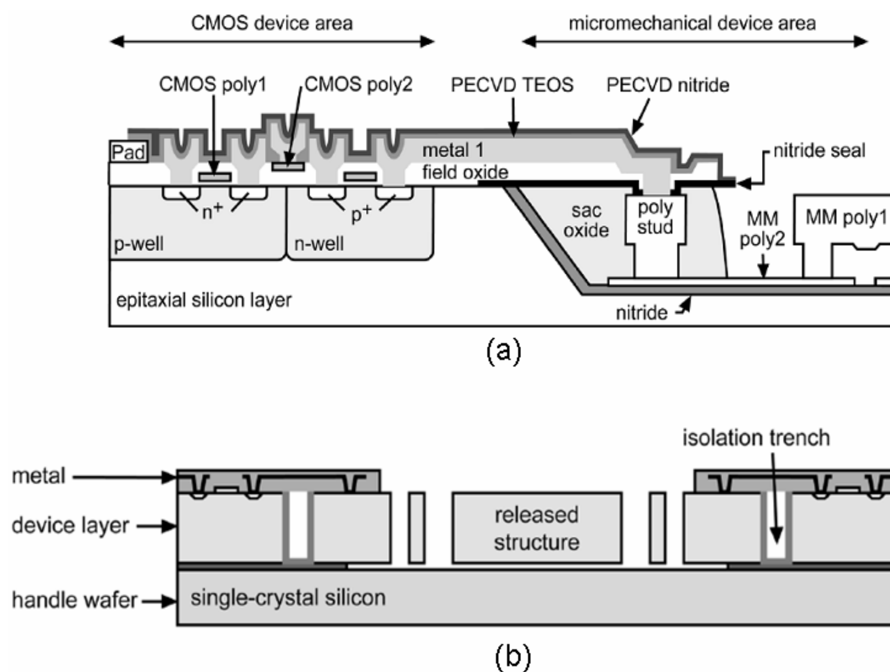


Fig. 2.1 Schematic cross-sectional views of two pre-CMOS MEMS processes: (a) M$^3$EMS technology developed by Sandia National Laboratories [47]. (b) SOI MEMS with 10 μm device layer for fabrication of single-crystalline silicon inertial sensors [52].

### 2.2.1 INTRA-CMOS

In the intra-CMOS approach, the CMOS process sequence is interrupted for additional thin film deposition or micromachining steps. This approach is

commonly exploited to implement surface micromachined polysilicon structures in CMOS technology. Either the standard gate polysilicon or an additional low-stress polysilicon layer is used as structural material. Intermediate micromachining is most commonly used to integrate polysilicon microstructures in CMOS/BiCMOS process technologies. Inserting the micromachining process steps before the back-end interconnect metallization ensures process compatibility with the polysilicon deposition and anneal. The polysilicon annealing temperature is typically limited to about 900 ºC in order not to affect the doping profiles of the CMOS process. Commercially available examples of polysilicon microstructures, fabricated with CMOS/BiCMOS processes with intermediate micromachining, include Analog Devices ADXL series accelerometers and ADXRS series gyroscopes [55], Infineon Technologies' KP100 series pressure sensors [56] and Freescale's (Motorola) MPXY8000 series pressure sensors [57]. Fig. 2.2 shows two cross-section of intra-CMOS processes

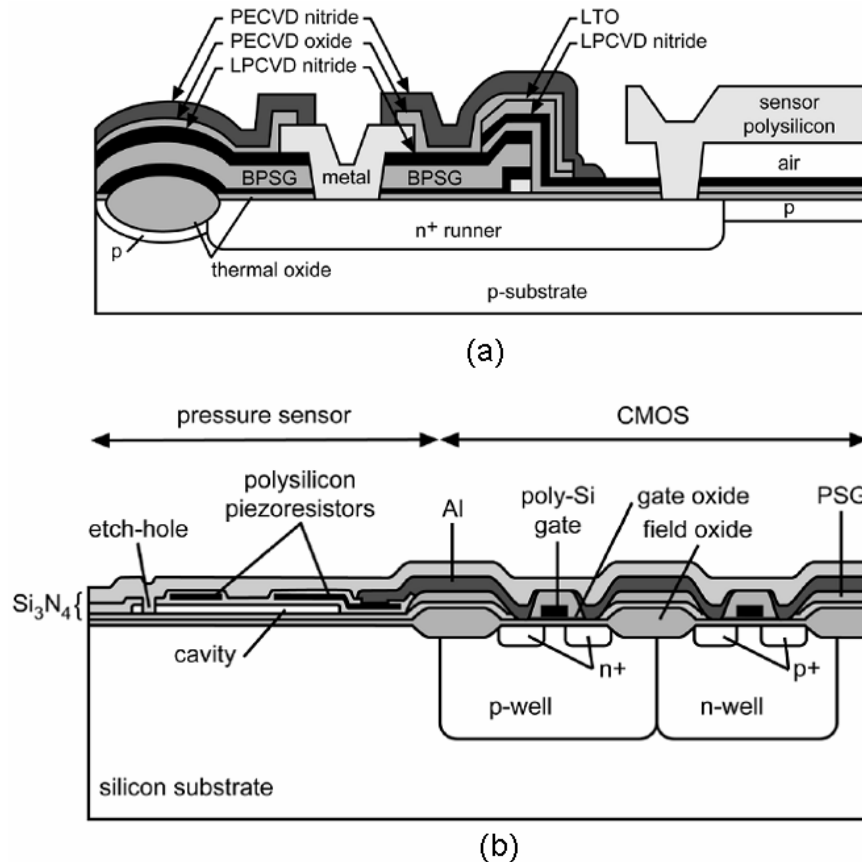


Fig. 2.2 Schmatic cross-sectional view of two intra-CMOS processes: (a) Analog Devices' integrated MEMS technology with an n+-diffusion interconnect structure between polysilicon microstructure and on-chip electronics [58].(b) Srface micromachined pressure sensor element developed at Toyota Central R&D Laboratories [59].

### 2.2.1 POST-CMOS

In the post-CMOS approach, two general fabrication strategies can be distinguished. In the first strategy, the MEMS structures are completely built on top of a finished CMOS substrate, leaving the CMOS layers untouched. Examples for this approach are Texas Instruments' Digital Micromirror Device (DMD) [60,61], the electroplated ring gyroscope developed by Delphi Automotive

Systems [62-64], the electroplated acceleration switch developed by Infineon [65,66], and Honeywell's thermal imagers [67]. In all four cases, the microstructures are released using sacrificial layer etching. Alternatively, the MEMS can be obtained by machining the CMOS layers after the completion of the regular CMOS process sequence. Using a variety of CMOS compatible bulk and surface-micromachining techniques, e.g., pressure [68-70], inertial [71], flow [72], chemical [73], and infrared radiation [74] sensors have been produced this way. Both post-CMOS approaches are attractive, because the CMOS wafers can be processed at any CMOS (or BiCMOS) foundry. This way, even very advanced CMOS technologies with multiple (copper) metallizations can be exploited for MEMS. The main limitation of the post-CMOS technologies is the stringent thermal budget for the add-on fabrication steps, limiting process temperatures to about 400 "C. Fig. 2.3 illustrates the cross-sectional views of two different post-CMOS processes.

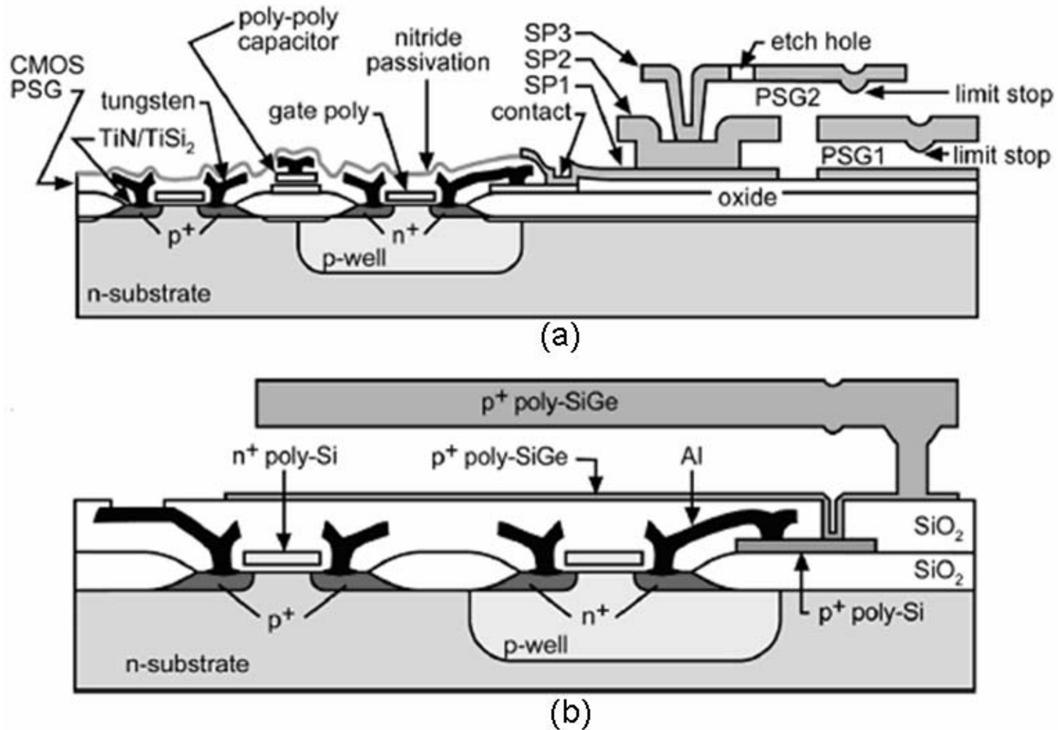


Fig. 2.3 Schematic cross-sections of (a) polysilicon and (b) polycrystalline silicon germanium (poly-SiGe) microstructures fabricated by post-CMOS surface micromachining techniques on top of a completed CMOS substrate wafer [75,76].

## 2.3 Fabrication Processes

The CMOS processes and post-CMOS micromachining steps utilized to fabricate the proposed devices are described in the following two sections.

### 2.3.1 CMOS Fabrication Process

The beginning of the CMOS processes is a lightly p-doped (110) wafer with a typical doping concentration of $N_A$~$10^{15}$. The first step is the definition of the active areas by local oxidation of silicon (LOCOS), thus growing a thick (~0.4 μm) field oxide in the areas between the individual transistors. Next, the p-wells for the n-channel MOSFETs and the n-wells for the p-channel MOSFETs are

impla[1]nted. A joint drive-in for both wells establishes the desired junction depth of 2–3 μm. Typically, drive-in times are 4–6 h at 1000-1100 ℃. The n-well diffused in the p-substrate can be used to define accurately the thickness of a silicon membrane. Such membranes are commonly released by anisotropic wet etching from the back of the wafer using an electrochemical etch-stop technique at the p-n junction between n-well and p-substrate.

After n- and p-well formation, the MOSFET gate and channel regions are engineered. First, Channel implants for the n- and the p-channel transistors are implanted to adjust their threshold voltage to the desired values. After removing the implantation oxide in the active area, the fate oxide with a thickness ≦ 10 nm in modern CMOS process is thermally grown in the active areas. Next, a 0.3–0.5 μm thick polysilicon layer for the gate electrodes is deposited across the wafer in an LPCVD furnace operating at about 600 ℃ and doped by ion implantation. Finally the polysilicon layer is patterned to define the actual gate regions. In MEMS, the gate polysilicon can also be used for resistors, pizoresistors, thermopiles, electrodes, and as structural materials. The last application often requires a high-temperature anneal of the polysilicon to reduce its residual stress to values acceptable for the microstructures. Such a high temperature step can be critical at this stage in the CMOS process, as it might effect previous doping distributions and, hence, the CMOS device characteristics.

After gate formation, the source/drain regions are implanted. In typical sub-micro CMOS technologies, this is done using a LDD (light doped drain) process. It provides a gradient in the doping of the source/drain regions towards the channel region, reducing the peak value of the electric field close to a channel and, hence, increasing device reliability. First phosphorus (or arsenic as alternative

[*] Appendix A: CMOS Process Flow

n-type dopant) is implanted in the source/drain of the NMOS transistors to form $n^-$ regions, followed by a boron implantation of the source/drain of the PMOS transistors to form $p^-$ regions. Next, a conformal spacer dielectric layer is deposited on the wafer and anisotropically etched back, leaving sidewall spacers along the edges of the polysilicon gate. After growing a thin screen oxide for the following implantation, the wall spacer of the source/drain region of the NMOS and PMOS transistors not protected by the sidewall spacer are successively implanted to form $n^+$ and $p^+$ regions, respectively. The final step of the source/drain engineering is a furnace anneal, typically at ~ 900 ℃ for 30 min, to activate the implants, anneal implant damage, and drive the junctions to their final depth. Alternatively to the furnace anneal a much shorter rapid thermal anneal at higher temperatures can be performed (e.g. 1 min at 1000–1050 ℃). The fabrication of the active devices is now completed. Any subsequent high-temperature step (above 700–800 ℃) necessary for the MEMS fabrication must be carefully qualified, as it night affect the doping distributions in the active devices, thus potentially changing the device characteristics.

In the back end of the process, the individual active devices are interconnected on the wafer to form circuits and pads for input/output connections off the chip are created. Although a large number of back-end metallization process flows with up to eight metallization levels exist, the CMOS processes described in this dissertation use four metallization levels. The contacts to the source/drain regions and to the gate polysilicon are based on tungsten (W) with a TiN (titanium nitride) adhesion/barrier layer. To planarize the surface of each layer, modern CMOS processes often use chemical mechanical polishing (CMP) for interconnect and interconnect dielectric planarization. Each of the following wiring levels uses CVD tungsten vias with a TiN adhesion/barrier layer and an

aluminum (with a small percentage of Si and Cu) interconnect layer. Finally, the passivation layer is deposited (typically by PECVD) and patterned to form the pad openings necessary to contact the device from the outside. The composition of the passivation layers are $SiO_2$ and $Si_3N_4$. After passivation, the wafers are annealed at low temperatures (400–500 ℃) for about 30 min in forming gas (10% $H_2$ in $N_2$) to alloy the metal contacts. The thickness of each layer is shown in fig. 2.4.

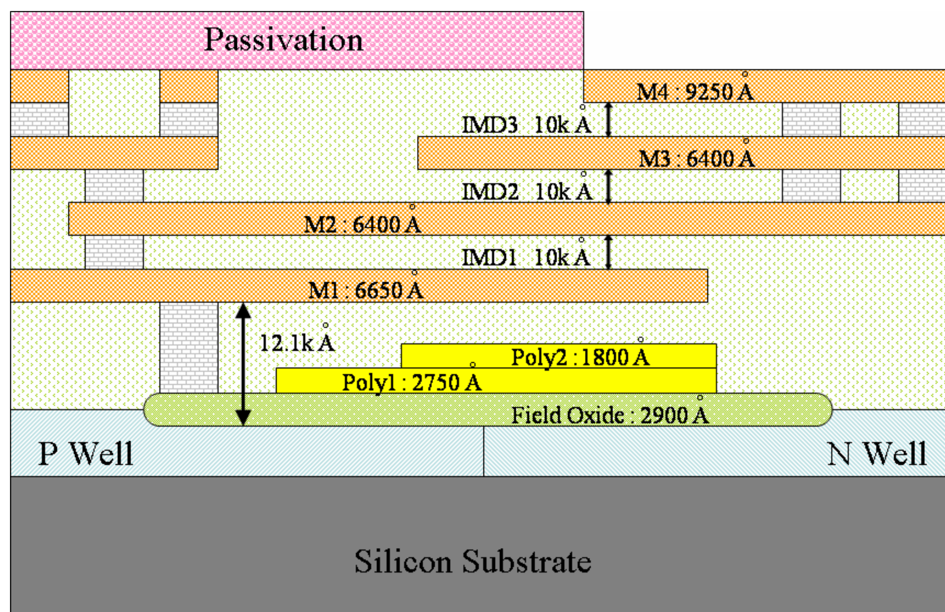


Fig. 2.4 Thickness of each layer for the TSMC CMOS process.

### 2.3.2 POST-CMOS MICROMACHINING STEP OF CIC

The CMOS processes make use of two polysilicon layers, four metal layers, three via layers, and several dielectric layers/sacrificial layers. The four metal layers are made of aluminum. The contact and via holes are filled with tungsten plugs, and the dielectric layers/sacrificial layers (IMD) are made of silicon dioxide. The field oxide layer (FOX) is made of silicon dioxide. The etched holes are filled with silicon dioxide. In order to make the plane surface flat, chemical and mechanical polishing (CMP) is employed after each layer is deposited. Fig. 2.5(a)

schematically shows a cross-sectional view of the MEMS components fabricated by the TSMC 0.35 μm 2p4m CMOS processes. Afterwards, post-CMOS micromachining steps are performed to release the suspension structures of MEMS devices by etching the silicon dioxide and silicon substrate. The release processes need an additional photomask to define the etching areas. First, a thick photoresist (PR) layer is coated on the chip and patterned, as shown in Fig. 2.5(b). This patterned PR mask is used to protect the bonding pads, electronic circuit, and the unneeded etched regions of the MEMS components during reactive-ion etching (RIE) process. Then, an anisotropic RIE with $CHF_3/O_2$ plasma is used to define the sidewalls of the device structure and etch the silicon dioxide in the etching holes. Fig. 2.5(c) schematically shows a cross-sectional view of a MEMS device after anisotropic RIE. Next, an isotropic RIE with $SF_6/O_2$ is performed to etch the silicon underneath and release the suspended structures of the MEMS components. Finally, the PR layer is removed and the post-CMOS micromachining steps are completed. Fig. 2.5(d) schematically shows a cross-sectional view of a MEMS device with released suspended structures after completing the post-CMOS micromachining steps.

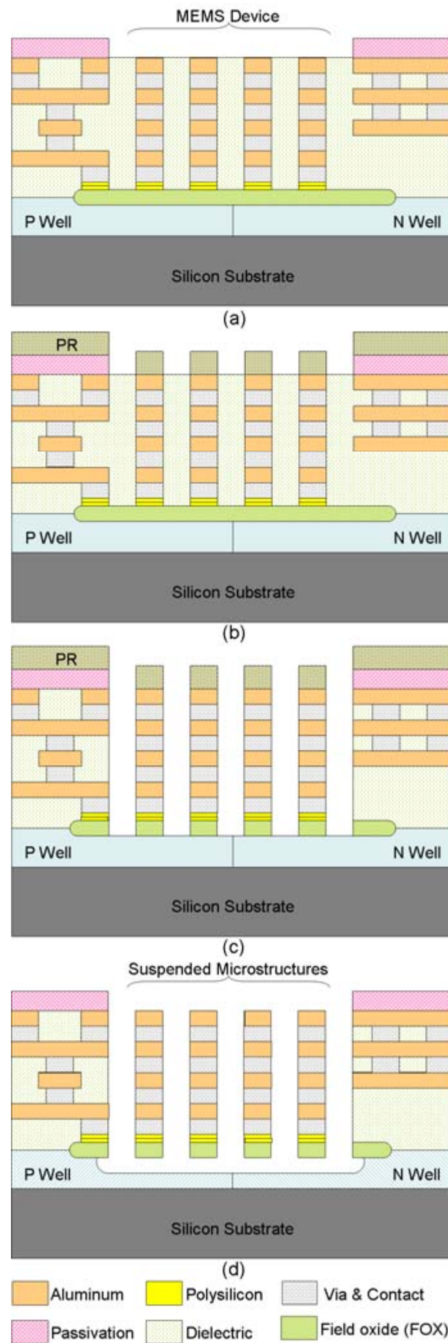


Fig. 2.5 Post-CMOS micromachining steps: (a) cross-sectional view of MEMS devices after completing TSMC 0.35μm 2P4M fabrication processes, (b) patterning of PR mask to protect unneeded etched regions, (c) performing anisotropic RIE to etch silicon dioxide, (d) cross-sectional view of device after completing post-CMOS micromachining steps.

# CHAPTER III

# CASCADE LATERAL ELECTROSTATIC COMB-DRIVE ACTUATOR

## 3.1 INTRODUCTION

Electrostatic comb-drive actuators have been developed and employed for many applications. However, side instability (side pull-in) limits the actuator stroke constraining its applications. Hence, extending stable traveling range is an important issue for designing electrostatic comb-drive actuators. In this chapter, a novel cascade electrostatic comb-drive actuator. Instead of shifting the spring constant of the suspended springs, the proposed actuator extends the stable traveling range using a multi-stage cascade configuration. To demonstrate the performance of the cascade configuration, simulation using the finite element method (FEM) simulation is utilized to model the proposed cascade actuator. Experimental results demonstrate that proposed design extends the stable traveling range of 200% as compared with a comb-drive actuator without this cascade configuration.

## 3.2 SIDE INSTABILITY OF LATERAL ELECTROSTATIC COMB-DRIVE ACTUATORS

Fig. 3.1 shows a conventional electrostatic comb-drive actuator. By applying a driving voltage between fixed comb fingers and movable comb fingers, the electrostatic force $F_x$ along the x-direction is

$$F_x = \frac{N\varepsilon t}{2g} V^2 \tag{3.1}$$

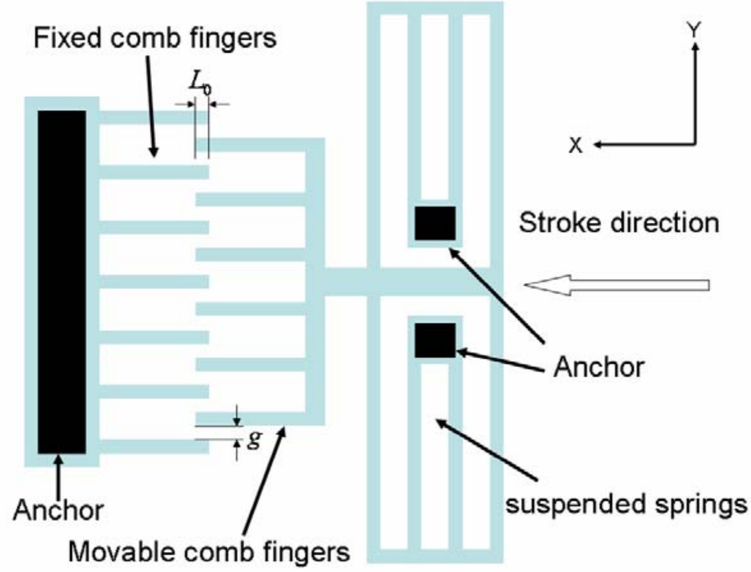


Fig. 3.1 Schematic drawing of a conventional electrostatic comb-drive actuator.

Here, $N$ is the number of finger pairs, $\varepsilon$ is the dielectric constant in air, $t$ is the finger thickness, and $g$ is the finger gap spacing. Ideally, the net electrostatic force $F_y$ along y-direction is zero. However, if movable comb finger structure moves a small displacement toward the fixed comb finger structure along the y-direction, the net electrostatic force $F_y$ is changed into

$$F_x = \frac{N\varepsilon t(L_0 + \delta_x)}{2(g-y)^2} V^2 - \frac{N\varepsilon T(L_0 + \delta_x)}{2(g+y)^2} V^2 \tag{3.2}$$

where $L_0$ is the initial overlap of the comb fingers, and the $\delta_x$ is the displacement of comb fingers in the x-direction, which is given by

$$\delta_x = \frac{N\varepsilon t}{2gK_x} V^2 \tag{3.3}$$

where $K_x$ is the spring constant of the suspension springs in the x-direction. This electrostatic force $F_y$ does not pull the movable comb finger structure back to

the original position, but pushes the movable comb finger structure further closed to the fixed comb finger structure. Hence, the movable comb fingers suddenly collide with the fixed comb fingers as shown in Fig. 3.2.

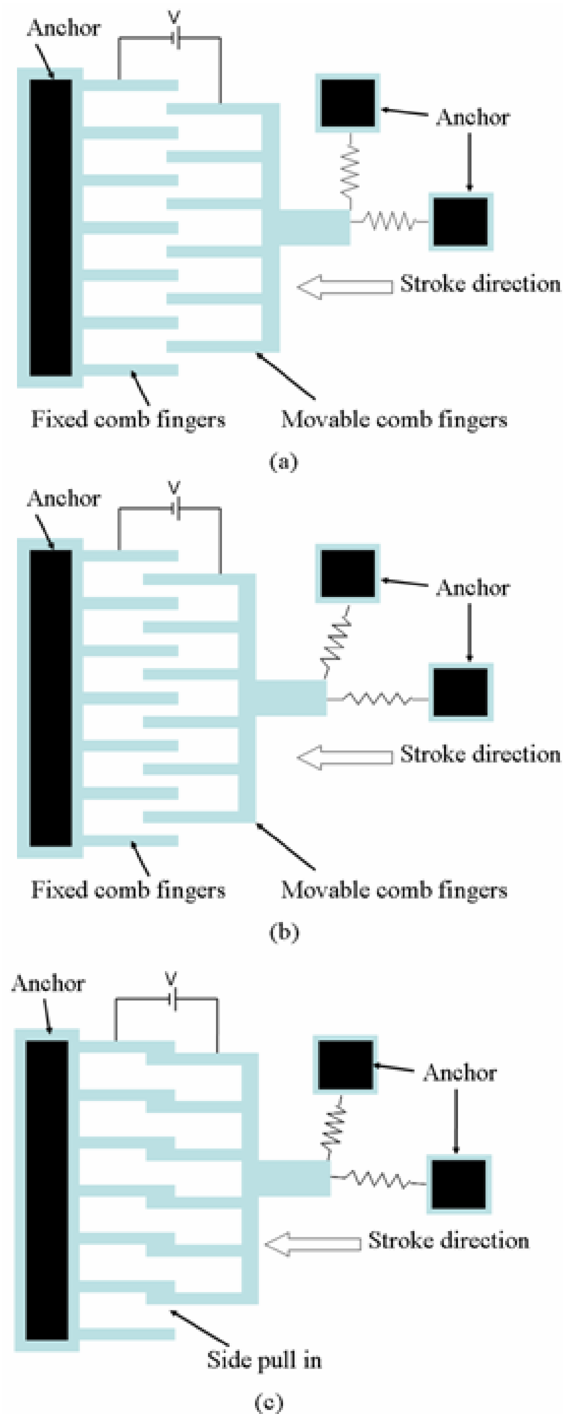


Fig. 3.2 Schematic drawings of an electrostatic comb-drive actuator (a) before actuation, (b) stable actuation condition, (c) side instability actuation condition.

This electrostatic force $F_y$ looks as if there was a “negative” spring and causes the actuator unstable. According to Hirano et al [77], the equivalent ‘negative” spring constant is defined as

$$K_e = \left.\frac{\partial F_y}{\partial y}\right|_{y=0} = \frac{2N\varepsilon t(L_0 + \delta_x)}{g^3} V^2 \tag{3.4}$$

The suspended springs could keep the moving comb finger structure against the instability of the electrostatic force. Hence, the stable condition of the comb-drive actuator is

$$K_y > \frac{2N\varepsilon t(L_0 + \delta_x)}{g^3} V^2 \tag{3.5}$$

where $K_y$ is the spring constant of the compliant suspension in the y-direction.

The most commonly used suspension in comb-drive actuators is the folded-beam flexure as shown in figure 1. The spring constants of the folded-beam flexure design in the *x*-direction and *y*-direction are [78]

$$K_x = \frac{2Ehb^3}{l^3} \tag{3.6}$$

$$K_y^{''} = \frac{2Eb}{l} \tag{3.7}$$

respectively, where $E$ is Young’smodulus, $b$ is the beam width, $h$ is the beam thickness, and $l$ is the length of one beam segment. According to Legtenberg *et al* [78], Eq. (3.7) is in fact the upper limit of the spring constant at zero displacement in the *x*-direction. It is important to note that the stiffness of the folded-beam flexure in the *y*-direction decreases with the increase of the displacement $\delta x$ in the *x*-direction. The displacement-dependent spring constant for the folded-beam flexure in the *y*-direction is given by [78]

$$K_y^{"} = \frac{200EI}{3\delta_x^2 l} \tag{3.8}$$

where $I$ is the second moment of inertia of the beam, $I = \frac{hb^3}{12}$. The total spring constant $Ky$ is then a series connection of the spring constant resulting from Hooke's law, i.e., Eq. (3.7), and the displacement-dependent spring constant resulting from equation 3.8.

The dashed lines in Fig. 3.3 show the analytical results of the spring constants $K_x$ and $K_x$ as functions of the displacement in the x-direction $\delta_x$. The length l, the width b, and the thickness h of the beams of the folded-beam flexure are 500, 3 and 2 µm, respectively. It is assumed that the actuator is fabricated using polysilicon, which is the most widely used material in MEMS. To predict the stable travel range of the comb-drive actuator with such folded-beam suspension, we also plot the equivalent 'negative' spring constant $K_e$ calculated from Eq. (3.4) as a function of the displacement $\delta_x$. The initial finger overlap $L_0$ and the finger gap spacing $g$ of the comb-drive are 5 and 2 µm, respectively. It can be seen that the stable travel range of such an actuator is about 33 µm. In Fig 3.3, we can also find that the maximum of the spring constant $K_y$ of the folded-beam suspension occurs when the displacement $\delta_x$ is equal to zero. However, in such a case, the equivalent 'negative' spring constant $K_e$ is small and reaches its minimum.

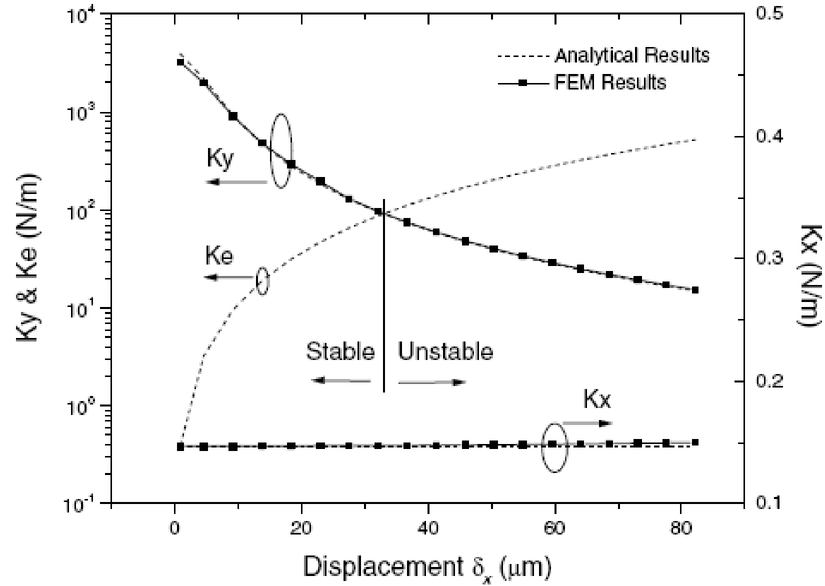


Fig. 3.3 Relationship between $K_e$, $K_x$, and $K_y$ [79].

From Eq. (5), it is clear that increasing the finger gap spacing $g$ increases the stable traveling range. However, increasing the finger gap spacing $g$ reduces the electrostatic force in x-direction that results in a higher driving voltage. Several approaches have been proposed to extend the stable traveling range [79–82]. Zhou and Dowd [79] used the tilted folded-beam suspended springs instead of the straight one to shift the spring constant in y-direction. The corresponding spring constant in y-direction changes from $\frac{200EI}{3\delta_x^2 l}$ to $\frac{600EI}{(3\delta_x - 5d)^2 l}$, where $E$ is Young's modulus, $I$ is the inertia moment of the mechanical spring, $d$ is the projection of the suspended beam length along the x-direction, and $l$ is the suspended beam length. Fig. 3.4(a) shows the schematic drawing of the electrostatic comb-drive actuator with tilted fold-beam suspended springs. Another approach to extend the stable traveling range is to adjust the length of the individual comb fingers and utilize pre-bent suspended springs. Grade et al [80] demonstrated the comb-drive actuator with pre-bent suspended springs and linearly engaging comb fingers, as shown in fig. 3.4(b). Recently, Hou et al [81]

utilized the secondly comb electrode to extend the stable traveling range. This approach could shift $K_e$ to extend the displacement of the electrostatic comb-drive actuator. Fig. 3.4(c) shows the configuration of an electrostatic comb-drive actuator with two sets of comb electrodes. Although these approaches could extend the stable traveling range, they need extra driving voltage to extend the stable traveling range.

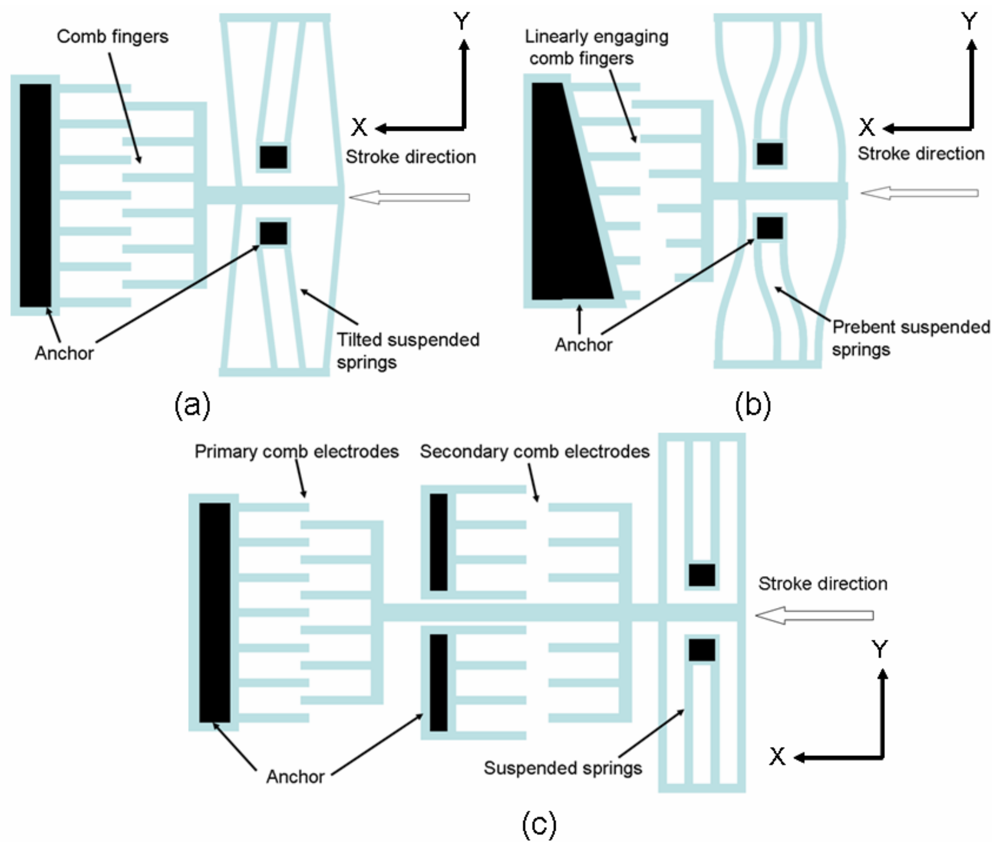


Fig. 3.4 Schematic drawings of (a) an electrostatic comb-drive actuator with tilted suspended springs [79], (b) an electrostatic comb-drive actuator with pre-bent suspended springs and linearly engaging comb fingers [80], (c) an electrostatic comb-drive actuator with two sets of comb electrodes [81].

## 3.3 Design of The Cascade Lateral Electrostatic Comb-Drive Actuator

### 3.3.1 Design concept

To extend the stable traveling range of the electrostatic comb-drive actuator without extra driving voltage, a novel electrostatic comb-drive actuator with a multi-stage cascade configuration is developed. Fig. 3.5 shows schematic drawings of the cascade comb-drive actuator. This actuator comprises three stages, where the $1^{st}$ stage is fixed and $2^{nd}$, $3^{rd}$ stages are movable. Each stage contains a fixed comb finger structure, a movable comb finger structure and suspended springs. The neighboring two stages are linked by the connection frame. This indicates that the movable comb finger structure of one stage is connected with the fixed comb finger structure of the next stage. Consequently, all of the three stages are constructed with a multi-stage cascade configuration. Notably, each comb-drive actuator could be driven independently. By applying driving voltage to each stage, the stroke of the cascade actuator is the summation strokes of the $1^{st}$, $2^{nd}$, and $3^{rd}$ stage respectively. Thus, the proposed cascade configuration actuator is capable of producing a stable extended traveling range.

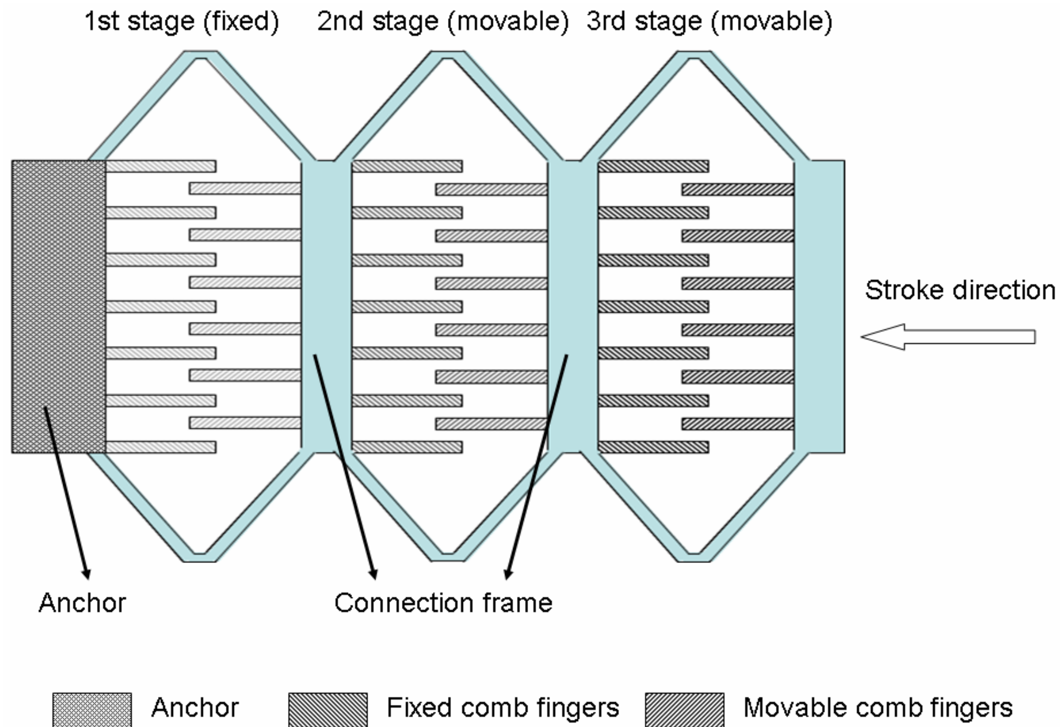


Fig. 3.5 Schematic drawings of an electrostatic comb-drive actuator with three actuation stages.

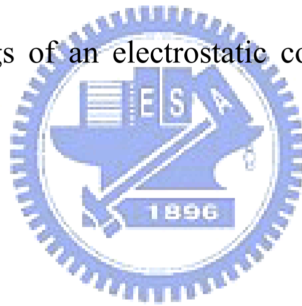


### 3.3.2 FEM SIMULATIONS

In order to verify the performance of the proposed multi-stage cascade configuration, a finite element method (FEM) simulator, IntelliSuite®, is employed to model the actuator. Fig. 3.6 and Fig. 3.7 show the 3D model of the electrostatic comb-drive actuator with a single stage and three stages, respectively. Fig. 3.8 shows the simulation result of an electrostatic comb-drive actuator with a single stage. The simulation result indicates the stroke of the actuator is 2.3 μm with 100V driving voltage. As shown in Fig. 3.9, by applying 100V driving voltage to each of the multi-stage cascade electrostatic comb-drive actuator, a displacement of 6.9 μm is obtained. The simulation results indicated that the actuator with three cascade stages extends the stroke three times as compared with

an actuator with only a single stage. Table 3.1 lists the parameter table of FEM simulations.

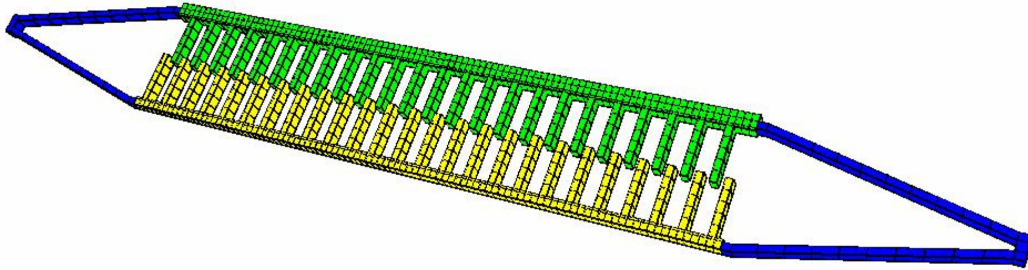

Fig. 3.6 3D model of the electrostatic comb-drive actuator with one stage.

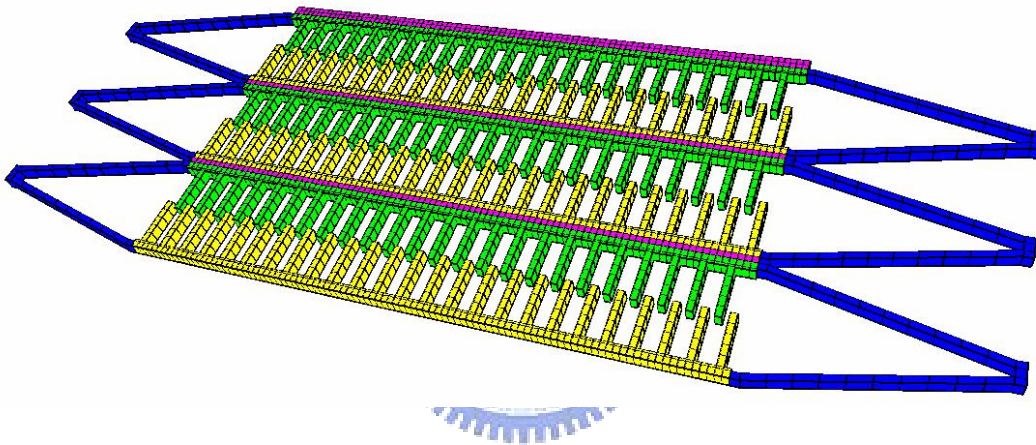

Fig. 3.7 3D model of the electrostatic comb-drive actuator with three stages.

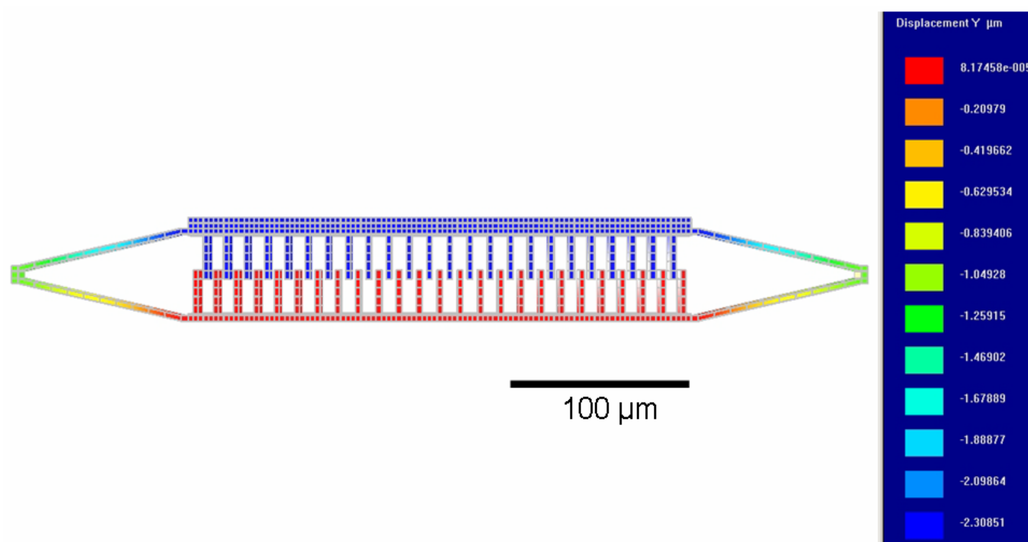


Fig. 3.8 FEM simulation results of an electrostatic comb-drive actuator with 100V driving voltage.

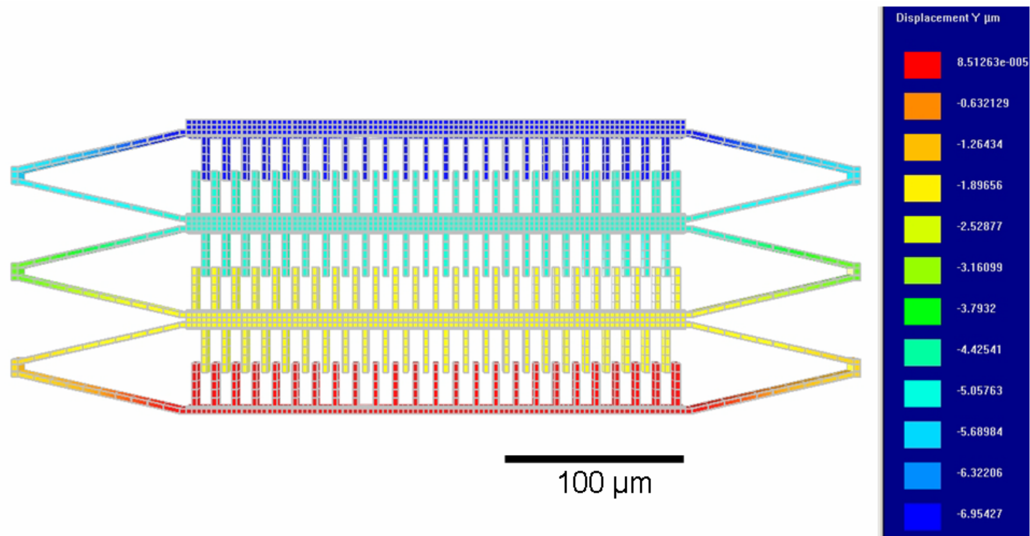


Fig. 3.9 FEM simulation results of a cascade electrostatic comb-drive actuator with 100V driving voltage.

TABLE 3.1: THE PARAMETER TABLE OF FEM SIMULATION

| | |
|---|---|
| Finger length | 25 µm |
| Finger width | 3 µm |
| Finger thickness | 6.5 µm |
| Finger gap | 3 µm |
| Fixed comb finger number | 24 |
| Fixed comb finger number | 25 |
| Young's modulus of aluminum | 64 GPa |
| Young's modulus of silicon oxide | 61 GPa |

### 3.3.3 ELECTRIC ISOLATION

As shown in fig. 3.10, the device fabricated by CMOS process consisted of several metal layers and dielectric layers. By performing post–CMOS micromachining steps, we are ale to release designed MEMS structure. With

multilayer structures, every part of the device can be connected electrically via the metal layers. As shown in figure 9, the fixed comb finger structure and movable comb finger structure are connected by the connection frame; however, the fixed comb finger structure and movable comb finger structure are electrically isolated by the dielectric layers. Hence, each stage of the cascade structure can be driven independently. To enhance the breakdown strength of the dielectric layer between the signal lines, M1 and M4 are employed as the actuation signal line; thus, a stacking dielectric layer, IMD1+IMD2+IMD3, design is utilized to increase the isolation thickness and raise the breakdown voltage between M1 and M4. As shown in figure 8, the thickness of IMD1+IMD2+IMD3 is 42.8k Å. Experimental results indicate that the stacking dielectric layer between M1 and M4 suffered no breakdown even with 200V driving voltage.

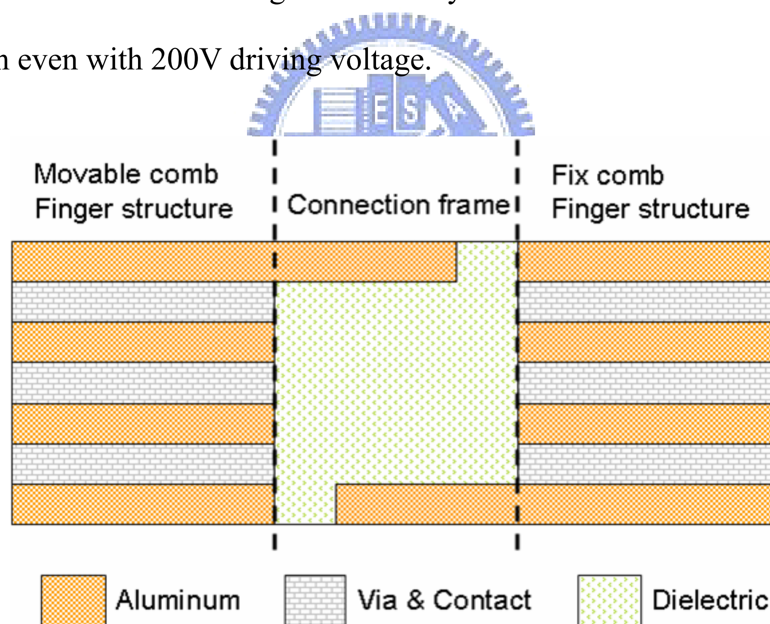


Fig. 3.10 Schematic Cross-section of movable comb finger structure, fixed comb finger structure, and connection frame.

## 3.4 EXPERIMENTAL RESULTS

Fig. 3.11 shows the scanning electron microscopy (SEM) image of the

fabricated device. The proposed cascade electrostatic comb-drive actuator consisted of three stages. Each stage comprises 24 movable comb fingers and 25 fixed comb fingers. The length and width of a comb finger are 25 μm and 3 μm, respectively. The finger gap spacing and the initial finger overlap are both 3 μm. The size of connection frame is 297× 12 $\mu m^2$.

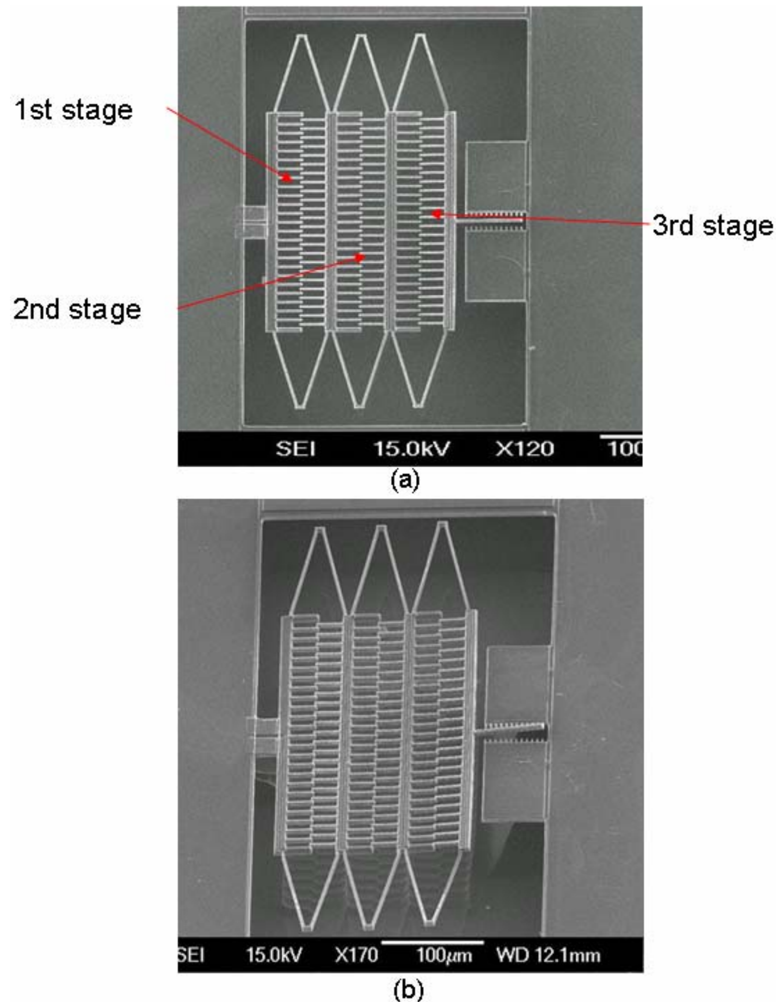


Fig. 3.11 The SEM image of the fabricated device (a) top view, (b) 45° view.

By applying driving voltage between move comb fingers and fixed comb fingers, we are able to measure the performance of the fabricated device by using an optical interferometric profiler (WYKO) as shown in Fig. 3.12. Fig. 3.13 shows the static characteristic of the fabricated device by driving each stage independently. The critical voltage for side pull-in is 125V. Before side pull-in

occurring, the maximum displacement of the 1st stage, 2nd stage, and 3rd stage are 3.6 μm, 3.4 μm, and 3.2 μm respectively. Since the dimension of each stage is designed to be the same; thus we are expecting the static characteristics of each stage should be the same. However, the measured static results of these three stages are different. It is due to the fact that the residual stress of the released device structure produced an out-of-plane bending as shown in Fig. 3.11(b). Fig. 3.14 shows the displacement versus DC driving voltage of the fabricated device by driving three stages simultaneously. With 125V driving voltage, the overall displacement of the actuator is 10.1 μm.

Fig. 3.12 The image of the optical interferometric profiler.

By comparing our experiment results with other approaches, the cascade structure can successfully extend the traveling range nearly 200% without the need of extra driving voltage. Note that the approaches using the tilted folded-beam suspension [79] and secondary comb electrodes [81] can extend traveling range up to 85% and 36%, respectively. This experiment result indicated that the design of cascade

structures is superior to previous designs in extending the traveling range.

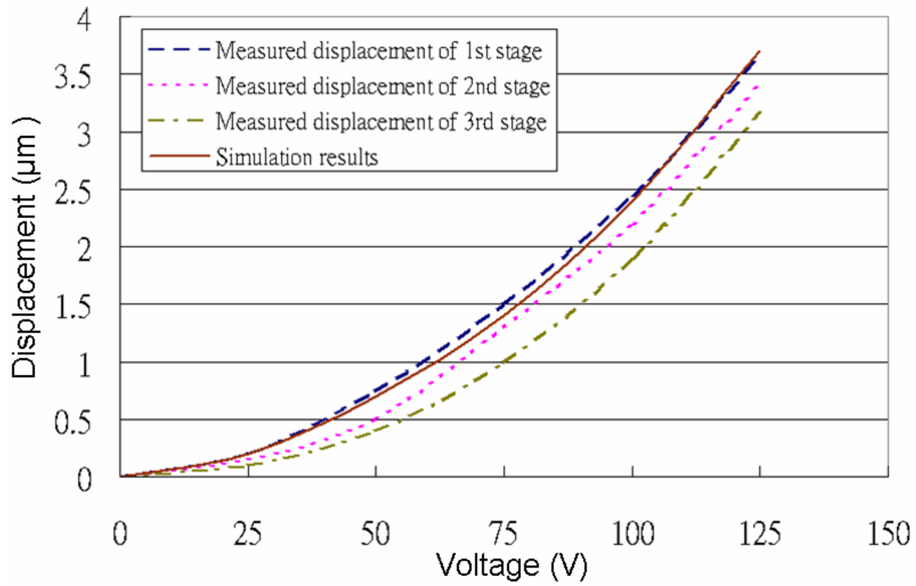


Fig. 3.13 The static characteristic of the design cascade electrostatic comb-drive actuator device. The solid line represents the simulation results of 1st stage, and the dash lines represent measured data of three different stage.

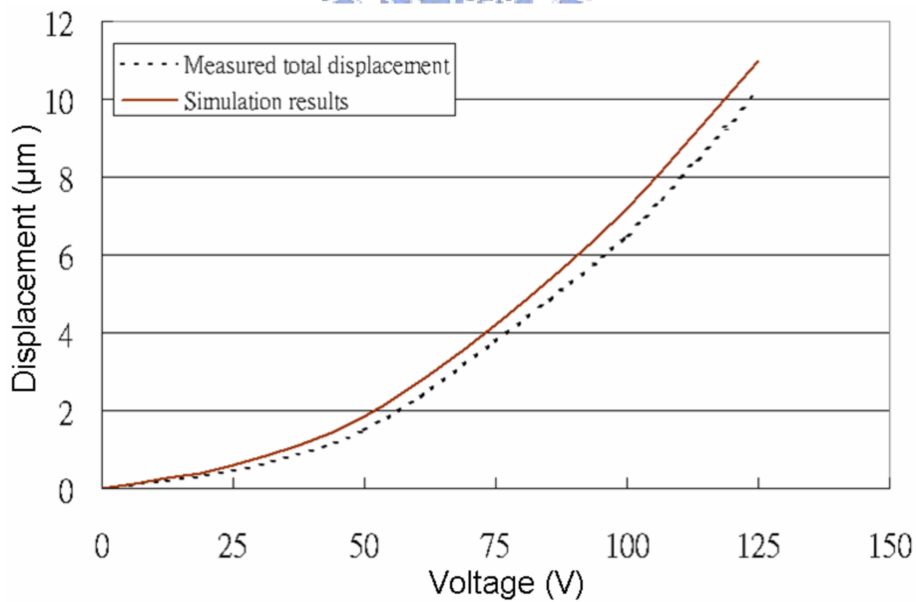


Fig. 3.14 The displacement versus driving voltage by driving three stages simultaneously. The solid line corresponds to simulation results, and dotted line corresponds to measured data.

## 3.5 Remark Conclusion

In this chapter, a novel cascade electrostatic comb-drive actuator is proposed. The simulation result, the fabrication process, and the experiment results are given to verify the proposed device. With this novel cascade configuration, the stable traveling range is extended successfully. Measurement results indicated that the proposed cascade actuator extends the stroke near 200% as compared with the actuator with single stage. This cascade electrostatic comb-drive actuator will benefit the microsystems that requires large traveling stroke such as micro x-y stages and variable optical attenuators.

# CHAPTER IV

# CASCADE VERTICAL ELECTROSTATIC COMB-DRIVE ACTUATOR

## 4.1 INTRODUCTION

In this chapter, a vertical electrostatic comb-drive actuator with a novel cascade configuration called cascade vertical comb-drive actuator (CVCA) is developed to magnify the actuation stroke. The CVCA combines vertical comb-drive actuators and multi-stage structures to form a stacked actuation configuration that can be used to overcome the stroke constraint of the traditional vertical comb-drive actuator. Due to the multilayer characteristic of the microstructure, the proposed CVCA can achieve the vertical motion and cascade structures. The experimental results indicated that the stroke of the proposed CVCA can be magnified three times as compared with that of the standard vertical comb drive with the same chip size.

## 4.2 SIDE INSTABILITY OF VERTICAL ELECTROSTATIC COMB-DRIVE ACTUATOR

The vertical motion of a verticval electrostatic comb-drive actuator occurs when a driving voltage is applied between the fixed comb fingers and the movable comb fingers. The electrostatic force of a comb finger pair is

$$F = \frac{\varepsilon l}{g} V^2, \tag{4.1}$$

where $\varepsilon$ is the dielectric constant in air, $l$ is the finger length, $g$ is the finger gap spacing, and $V$ is the applied voltage. Fig. 4.1(a) shows the schematic drawing of a vertical electrostatic comb-drive actuator without applying driving voltage. As the driving voltage between the fixed comb fingers and the movable fingers increases, the comb fingers become partially engaged, as shown in Fig. 4.1(b). As the driving voltage further increases, the comb fingers become fully engaged, as shown in Fig. 4.1(c). Therefore, the comb finger thickness $d$ is an important factor to improve the stroke of the vertical electrostatic comb-drive actuator and that actuation stroke increases while the comb finger thickness $d$ increases.

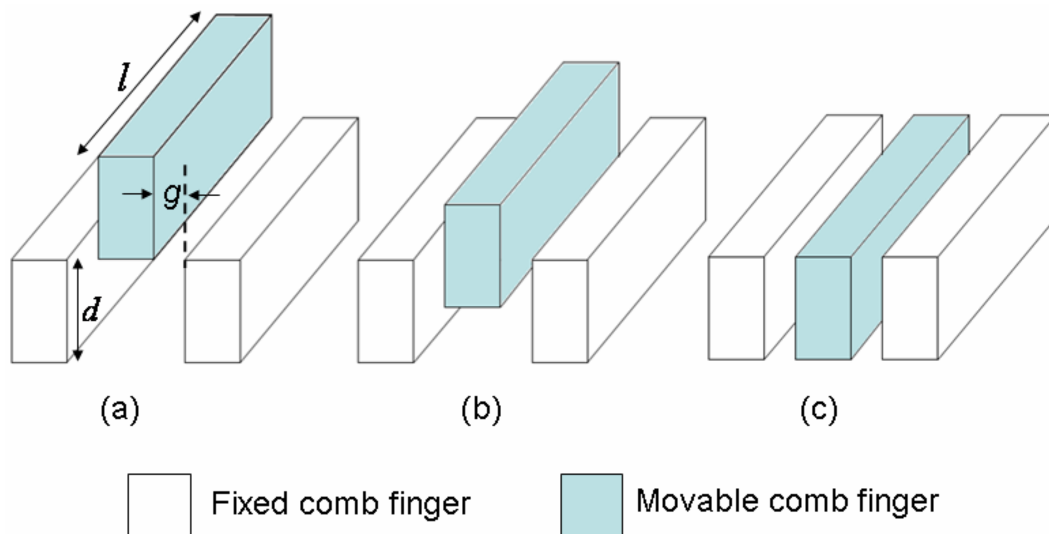


Fig. 4.1 Schematic drawing of comb fingers (a) not engaged, (b) partially engaged, and fully engaged.

To increase the stroke of typical vertical electrostatic comb-drive actuators, high-aspect-ratio micro-machining processes using electroplating, deep reactive iron etching (DRIE) or inductively coupled plasma (ICP) have been demonstrated [83–86]. Although these approaches can increase the actuation stroke, they often

need a complex fabrication process. In addition, vertical electrostatic comb-drive actuators with thick comb fingers easily result in side pull-in (side instability) [87]. Side pull-in means the situation in which the movable comb fingers move perpendicular to the stroke direction and then make contact with the fixed comb fingers. When comb fingers are increasingly engaged, the electrostatic force between the fixed comb fingers and the movable comb fingers becomes larger. If the movable comb fingers move with a small displacement along the x-direction, the movable comb fingers will suddenly snap to the fixed comb fingers. This so-called side pull-in phenomenon constrains the actuation stroke of the verticval electrostatic comb-drive actuator. Fig. 4.2 shows a cross-sectional view of the side pull-in condition. Therefore, increasing the comb finger thickness $d$ does not increase the actuation stroke with sufficient efficiency due to the side pull-in phenomenon.

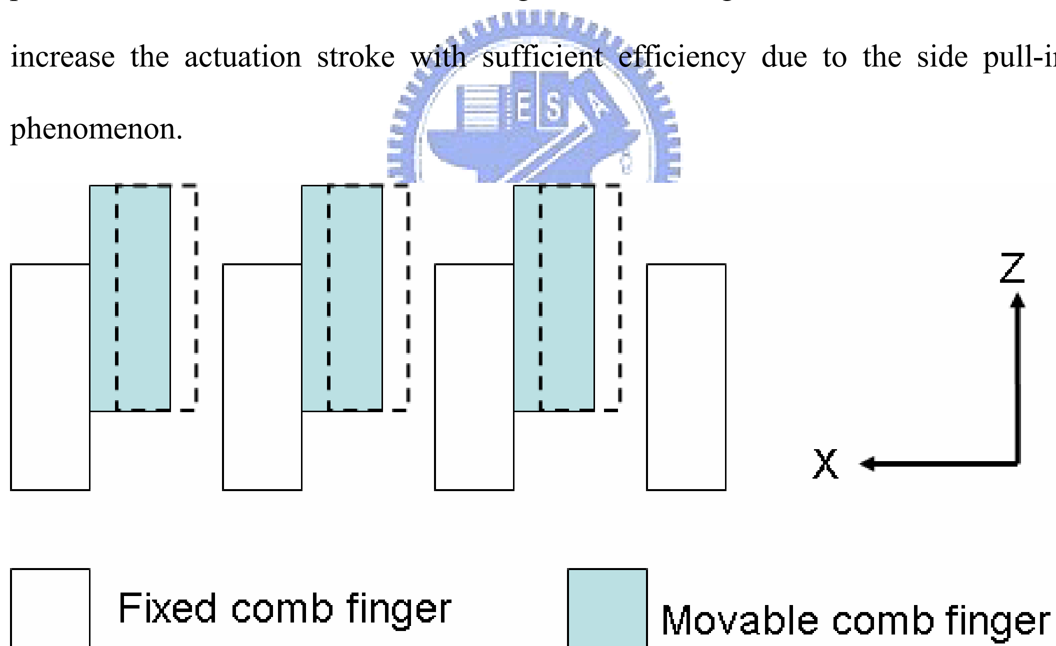


Fig. 4.2 Cross-sectional view of side pull-in condition.

## 4.3 DESIGN CONCEPT AND FEM SIMULATION

### 4.3.1 DESIGN CONCEPT AND FEM SIMULATION

To magnify the stroke of a vertical electrostatic comb-drive actuator, a vertical comb-drive actuator with a cascade configuration is developed. Fig. 4.3 shows a schematic diagram of a CVCA. This actuator comprises four stages, where the first stage is fixed to the anchor and second to fourth stages are connected to the neighbor stage. Each stage contains a fixed comb finger structure, a movable comb finger structure, and suspension springs. The neighboring two stages are linked by the connection frame. This indicates that the movable comb finger structure of one stage is connected with the fixed comb finger structure of the next stage. Consequently, all of the four stages are constructed with a multi-stage cascade configuration. Notably, each comb-drive actuator could be driven independently. By applying driving voltage to each stage simultaneously, the stroke of the cascade actuator is the summation strokes of the first, second, third, and fourth stages. Thus, the proposed CVCA is capable of performing a stable extended traveling range. Figure 4.4 shows the finite element method (FEM) simulation results of the simplified CVCA model.

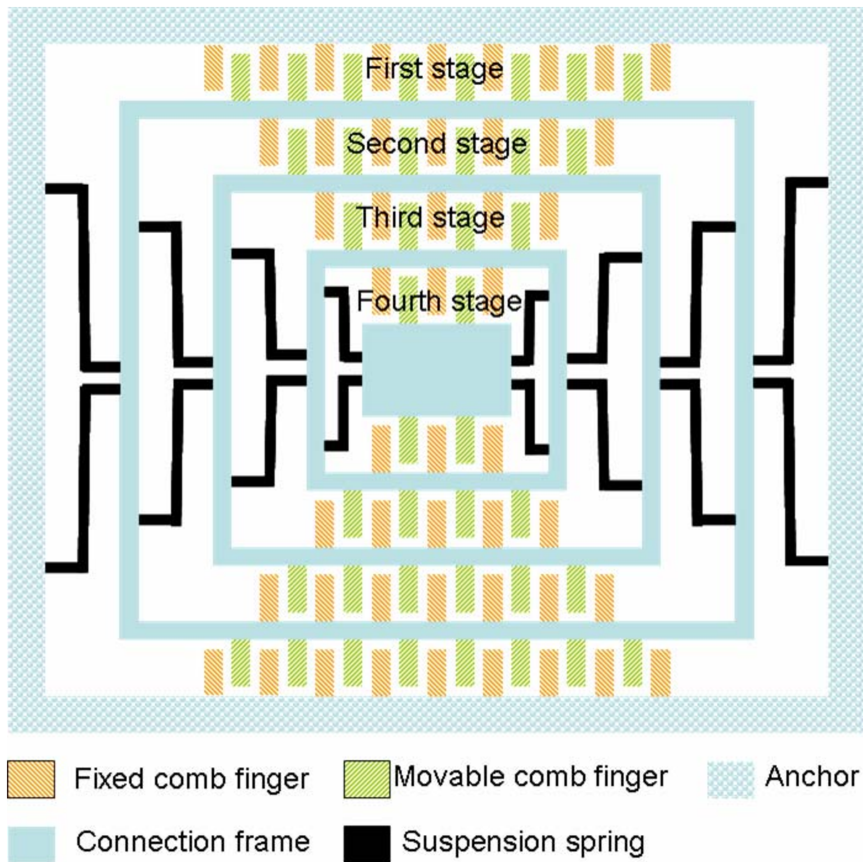


Fig. 4.3 Schematic drawing of CVCA with four stages.

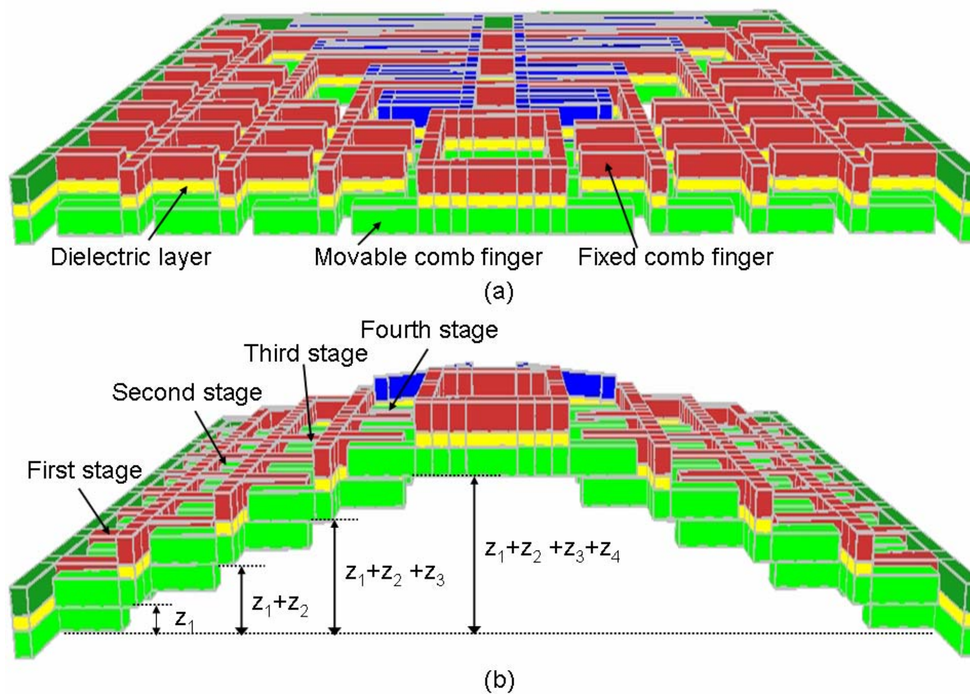


Fig. 4.4 FEM simulation results of simplified CVCA model (a) without driving voltage and (b) with driving voltage.

### 4.3.2 ACTUATION PRINCIPLE

As shown in Fig. 2.4, the microstructure can have several metal layers embedded, which is a major difference from homogeneous silicon counterparts. These characteristic multilayer structures enable the CVCA to have the vertical motion capability. Fig. 4.5 shows cross-sectional views of the fixed comb fingers and movable comb fingers. The fixed comb fingers comprise M3, M4, via, and silicon dioxide, and the movable comb fingers comprise Poly2, M1, M2, M3, via, and silicon dioxide. By applying driving voltage between the movable comb fingers and the fixed comb fingers, the actuator can achieve vertical motion due to the electrostatic force.

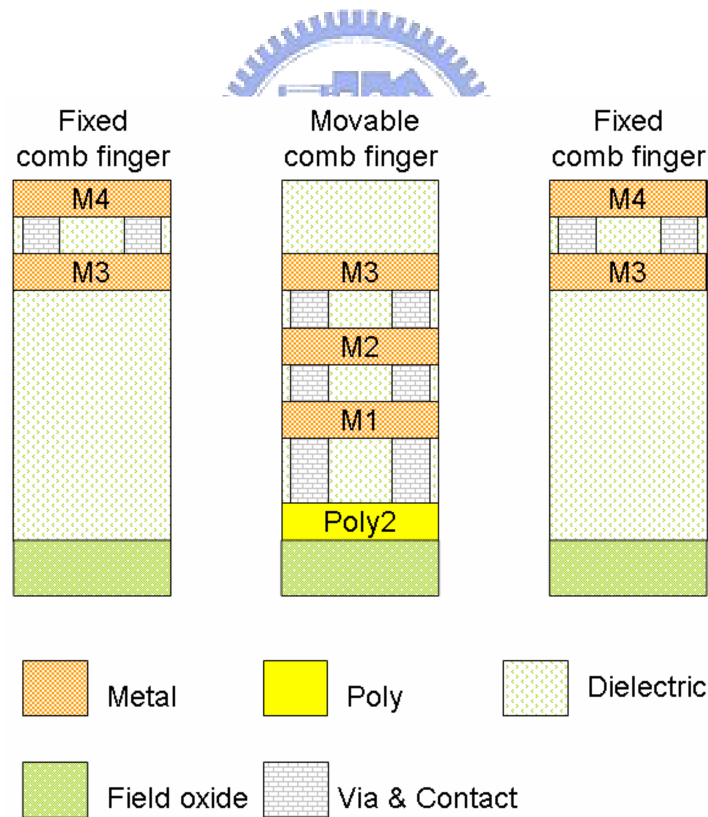


Fig. 4.5 Cross-sectional view of fixed comb fingers and movable fingers.

## 4.4 EXPERIMENT RESULTS

Fig. 4.6 shows a scanning electron microscopy (SEM) image of the fabricated CVCA. The proposed CVCA consists of four stages. The width and length of the comb fingers are 3.6 and 40 μm, respectively. The finger gap spacing and finger overlap are 3 and 35 μm, respectively.

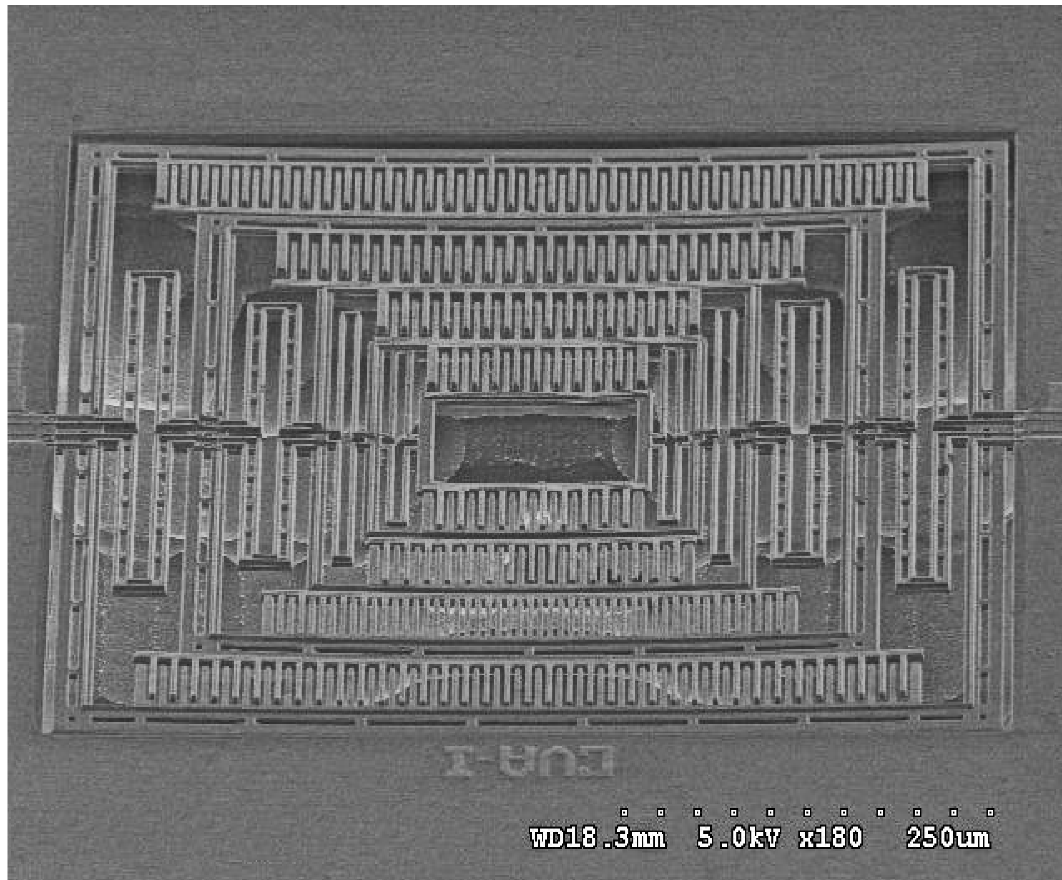


Fig. 4.6 SEM image of fabricated device.

By applying driving voltage between the movable comb fingers and the fixed comb fingers, we are able to measure the performance of the fabricated device using an optical interferometric profiler (WYKO). Fig. 4.7 shows the static characteristic of the fabricated device. The result indicates that the maximum total displacement that the CVCA (first stage + second stage + third stage + fourth

stage) can achieve is 2.6 μm by applying a 90 V driving voltage. Note that the displacement of the first stage is equivalent to the traditional vertical electrostatic comb-drive actuator, which can achieve 0.9 μm displacement with a 90 V driving voltage. In conclusion, the actuation stroke of the proposed CVCA can be magnify three times higher than that of the standard vertical comb drive actuator.

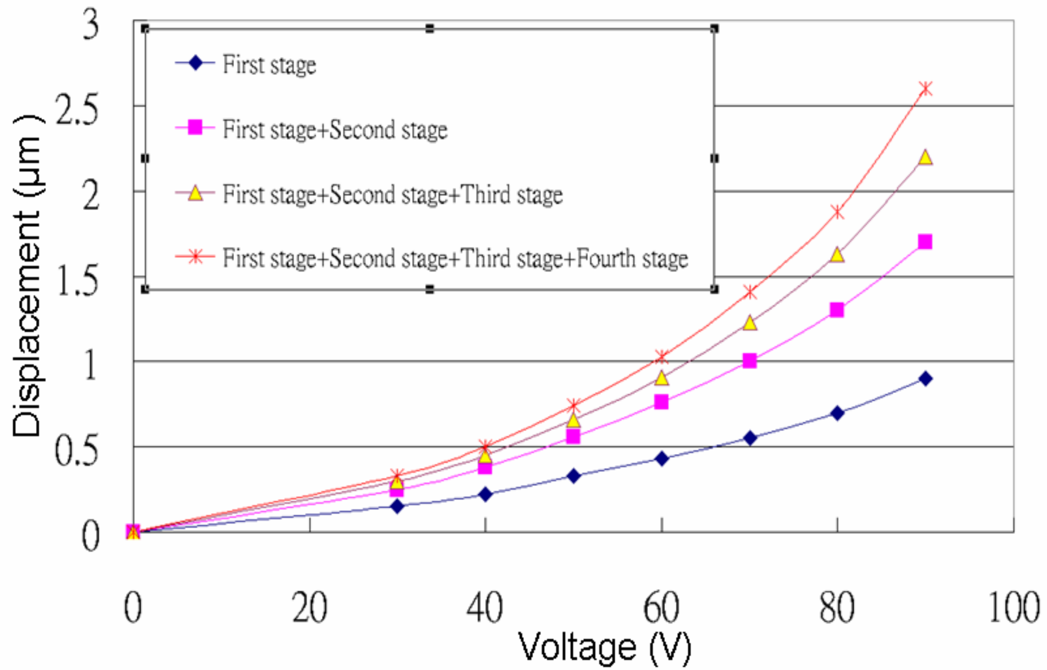


Fig. 4.7 Static characteristic of fabricated device.

## 4.5 REMARK CONCLUSION

A novel cascade configuration for magnifying the stroke of a vertical electrostatic comb-drive actuator is proposed in this paper. This novel design can be used to overcome the stroke constraint of a traditional vertical electrostatic comb-drive actuator. The proposed CVCA is implemented using TSMC 0.35 μm 2p4m CMOS fabrication processes and post-CMOS micromachining steps. The design, simulation and measurement are also presented. The experimental results

indicate that the stroke of electrostatic actuator can be effectively magnified using the cascade configuration. The CVCA will benefit microsystems such as an optical pickup and a variable optical attenuator.

E S A
1896

# CHAPTER V

# CONCLUSIONS

## 5.1 SUMMARY OF THIS DISSERTATION

In this dissertation, the electrostatic comb-drive actuator with multi-stage configuration is proposed. With this cascade structure, the stroke of the actuator can be greatly improved without adding extra driving voltage. This cascade structure can be utilized in lateral electrostatic comb-drive actuators; furthermore, it can also be employed in vertical electrostatic comb-drive actuators. Commercialized FEM tools have been employed to simulate actuator characteristics. To realize the designed actuators, a CMOS process and post-CMOS micromachining steps are employed. Experimental results had demonstrated our design concept. The major contributions of this dissertation are summarized in the following section.

## 5.2 CONTRIBUTIONS

The major contributions of this dissertation are summarized in the following:

(1) Enlarge the stroke of actuator

The proposed cascade electrostatic comb-drive actuator can enlarge the stroke of the actuator. Comparing with traditional actuator (without cascade configuration), the proposed lateral actuator can improve the stroke up to 180%, and the proposed vertical actuator can improve the stroke up to 188%. With more cascade stages, the stroke can be improved more.

(2) Extending actuation stroke without adding extra driving voltage

Although the actuation stroke can be extended by utilizing the pre-bent suspensions or adding the second electrode, the actuators still need higher driving voltage to extend the actuation stroke. However, with this novel cascade configuration, the actuation stroke can be extended greatly without extra driving voltage.

(3) Capability of integrating with on-chip circuitry

In this dissertation, the proposed two actuators were fabricated through standard CMOS processes and post-micromachining steps. Hence, the actuators not only can be fabricated through commercial processes, but also can on-chip integrate with circuitry.

(4) Characteristics of multilayer structures

Unlike the general MEMS devices made of homogeneous polysilicon, the proposed actuators can have several embedded metal layer. This multi-layer structure characteristic can benefit MEMS devices have more advantages such as the electric signal isolation and the vertical motion capability. Therefore, the MEMS devices can be applied in more fields.

## 5.3 SUGGESTIONS FOR FUTURE RESEARCH

In this dissertation, the cascade electrostatic comb-drive actuators are designed, developed, and implement. With the cascade configuration, the actuation stroke can be improved greatly without extra driving voltage. For the future research, a few suggestions are provided as following:

(1) Improve the fabrication process to reduce the residual stress.

(2) Develop the X-Y-Z stage by combine the proposed lateral actuator and vertical actuator.

(3) Integrate the proposed actuators with other CMOS components such as CCD to form a complete MEMS system for practical applications.

(4) Develop other cascade actuators such as cascade thermal actuators and cascade magnetic actuators.

# APPENDIX A: CMOS PROCESS FLOW

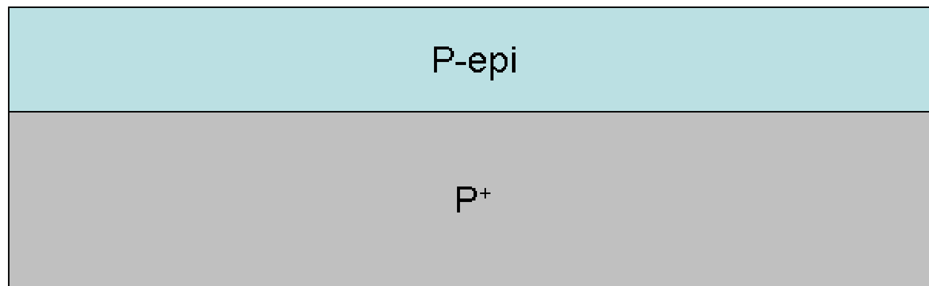


(a) Base material: $P^+$ substrate with P-epi layer.

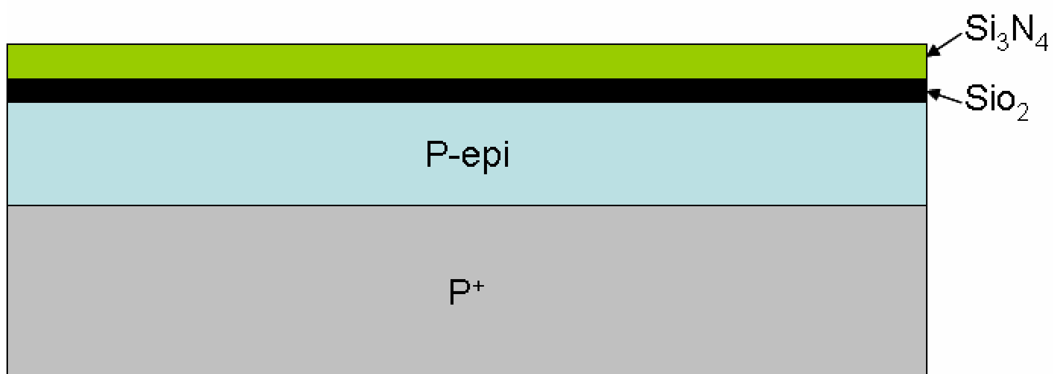


(b) After deposition of gate oxide, sacrificial nitride acts as a buffer layer.

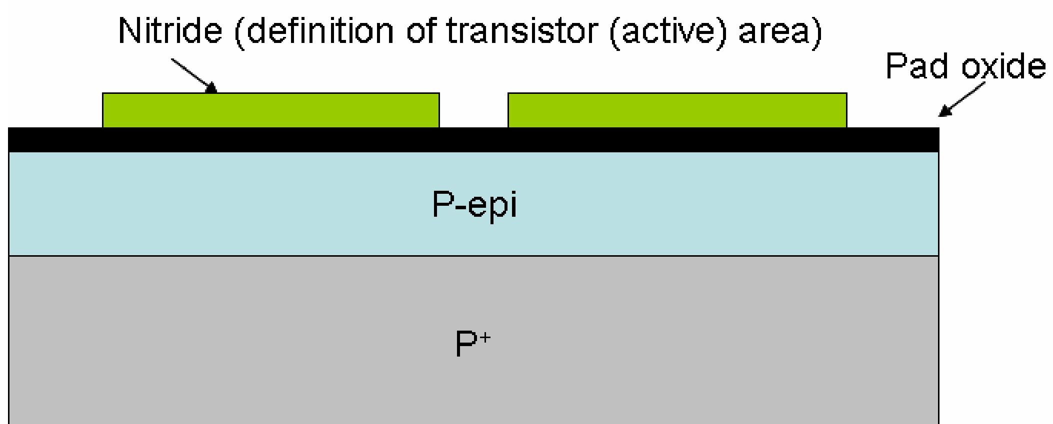


(c) After plasma etching of isolation trenches.

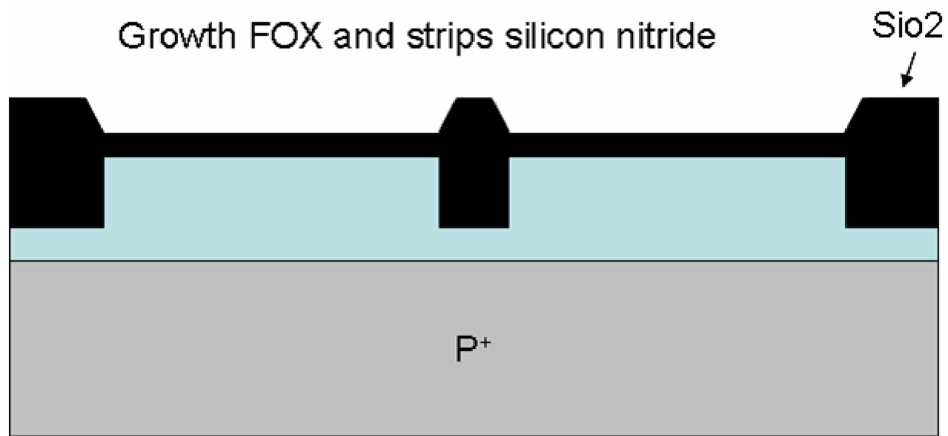


(d) After trenches filling, CMP planarization and remove of sacrificial nitride.

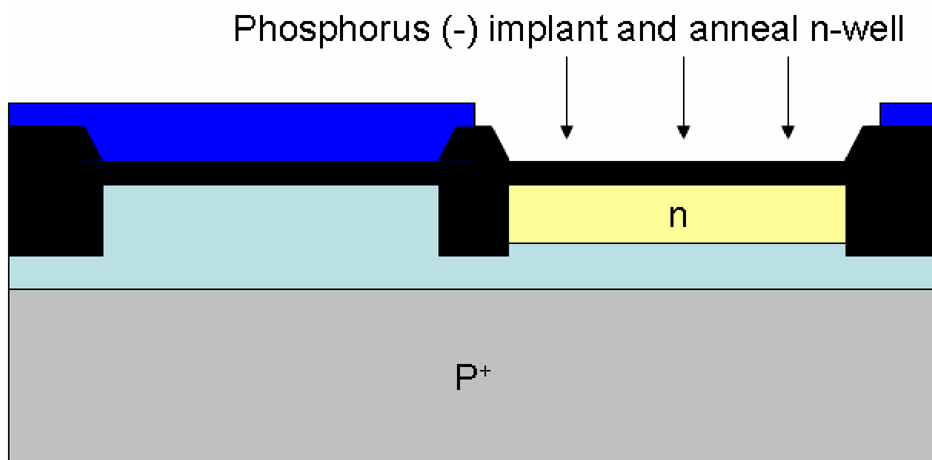


(e) After n-well implants.

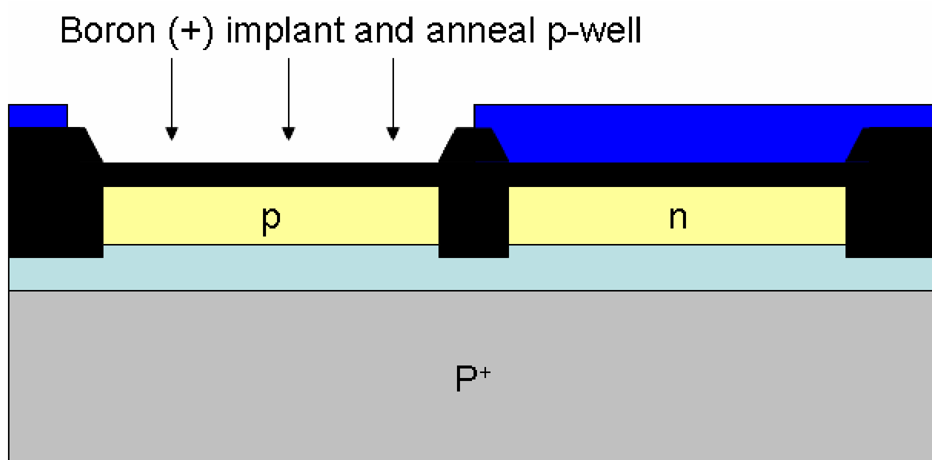


(f) After p-well implants.

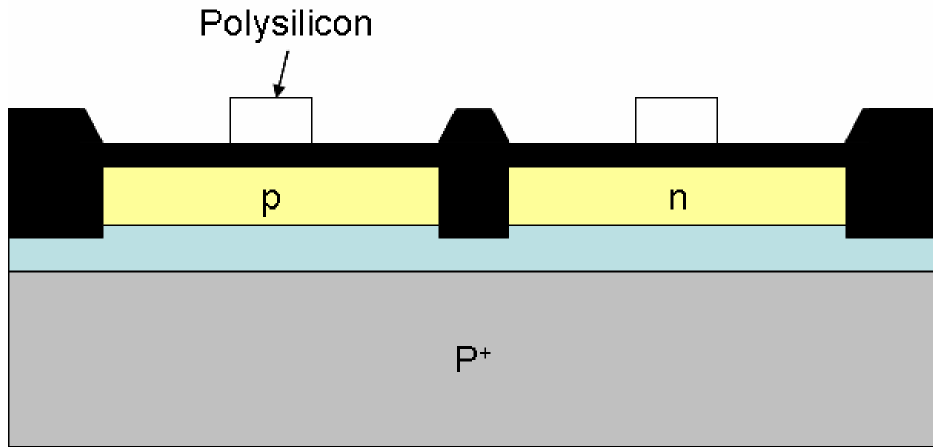


(g) After polysilicon deposition and etching.

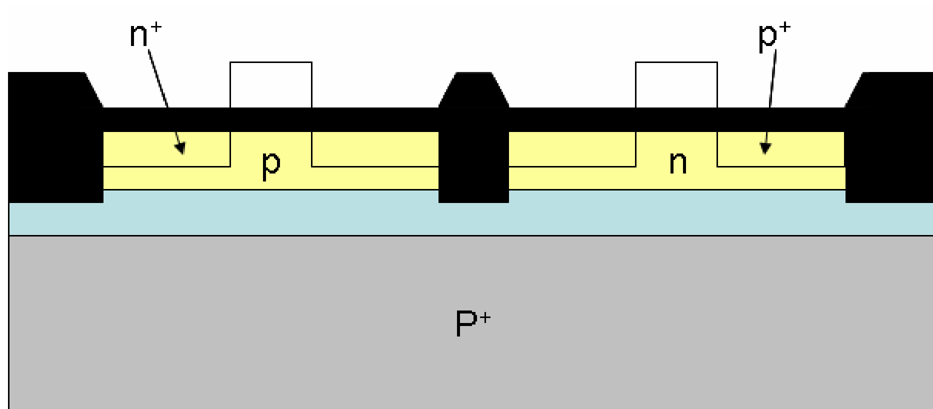


(h) After $n^+$ source/drain and $p^+$ source/drain implant.

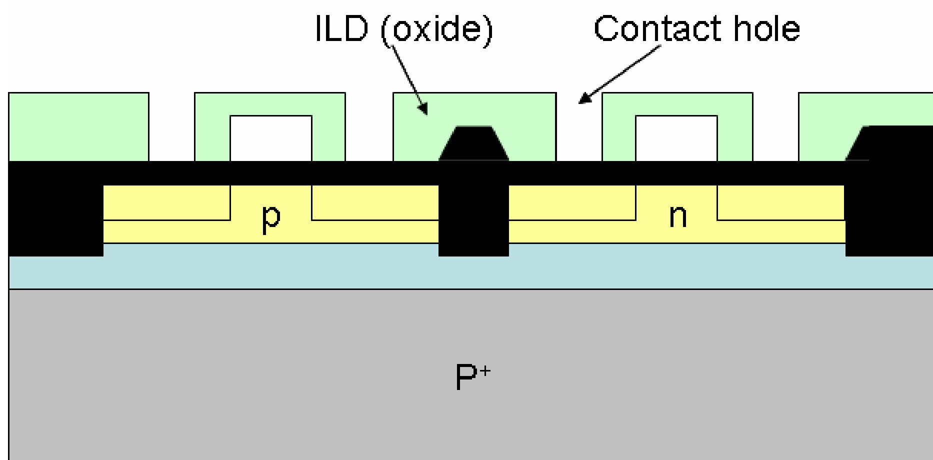


(i) After deposition and planarization (CMP) of inter-layer dielectric (ILD) layer, and pattern contact holes.

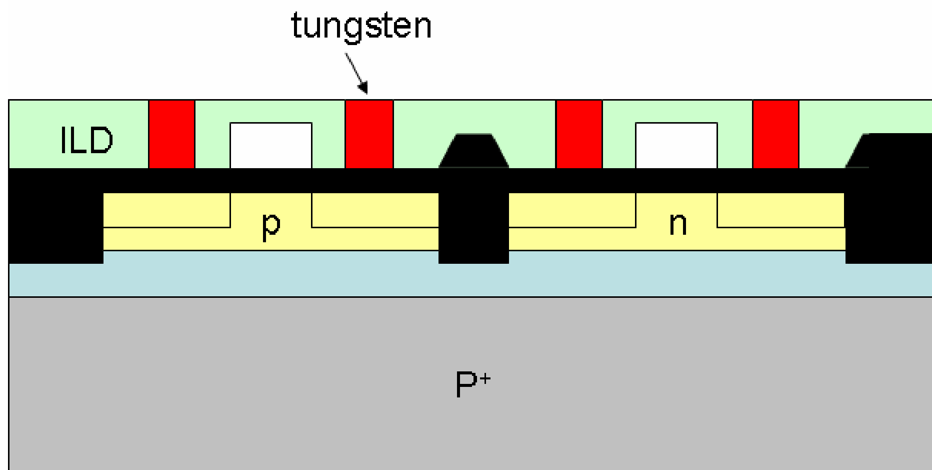


(j) Deposition and polish (CMP) the first tungsten layer.

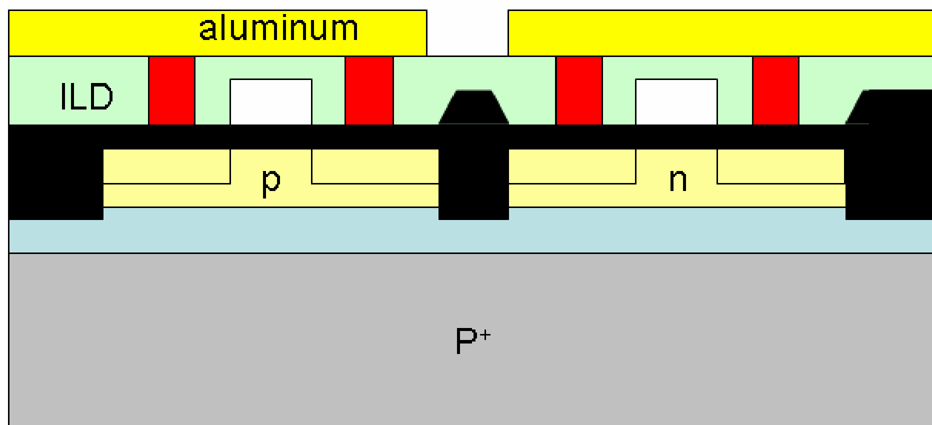


(k) After deposit and pattern the first aluminum layer.

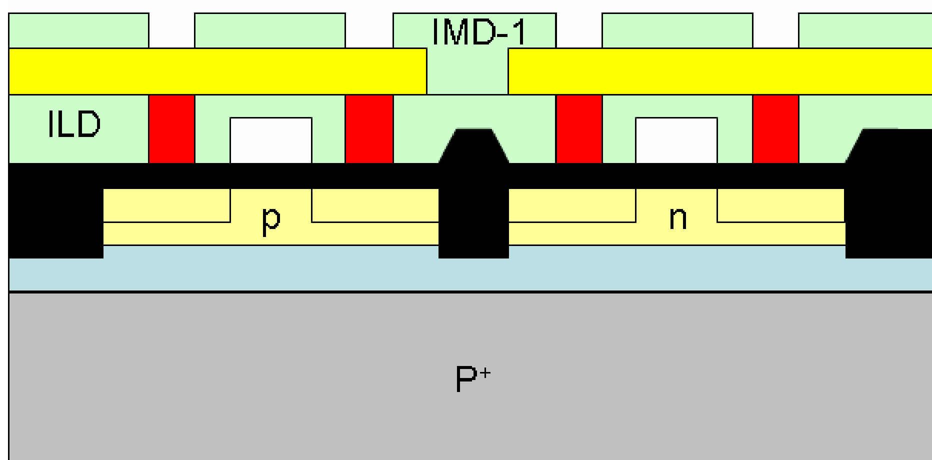


(l) After deposit and polish first inter-metal dielectric (IMD) layer (oxide), and pattern via holes.

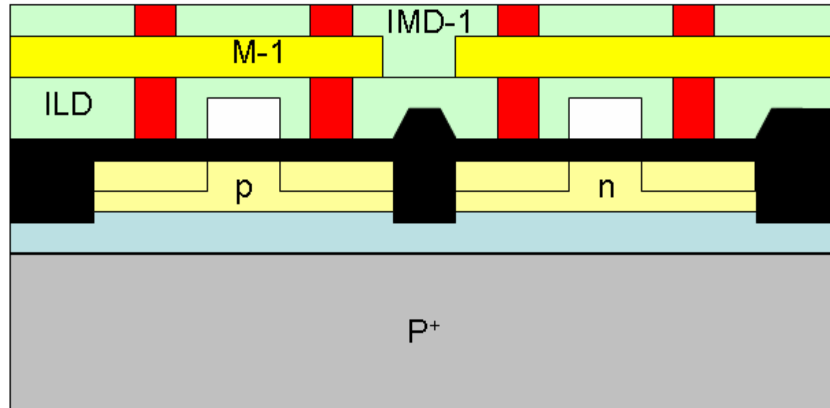


(m) After deposit the and polish second tungsten layer.

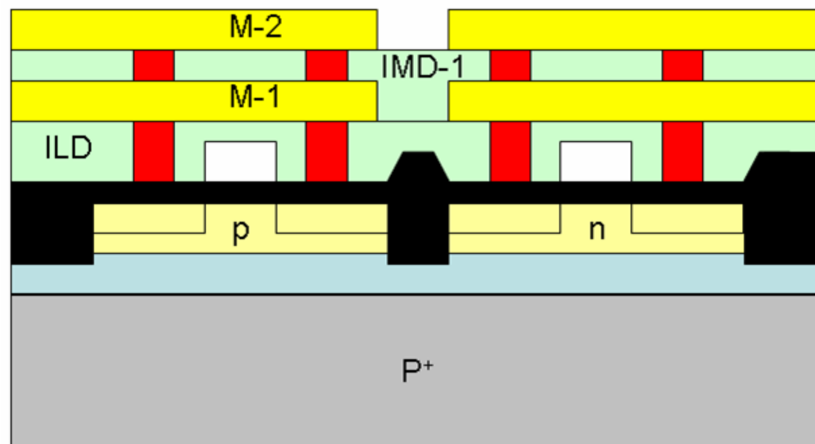


(n) After deposit and pattern the second aluminum layer.

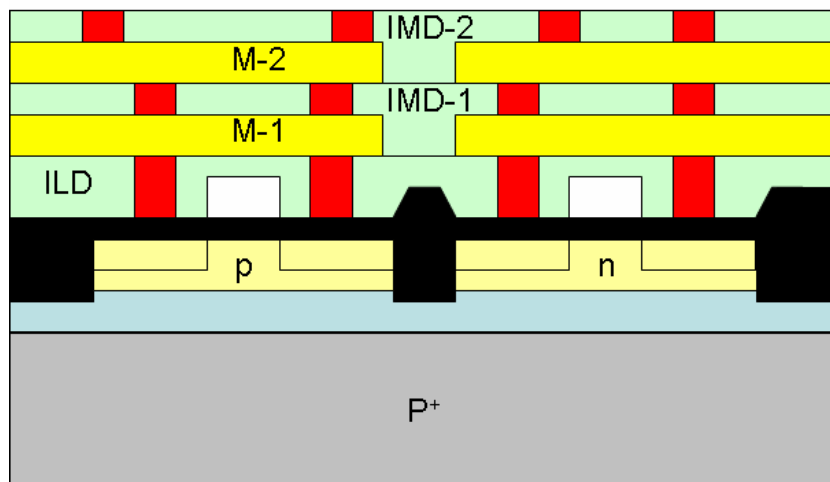


(o) After deposit the second IMD layer and the third tungsten layer

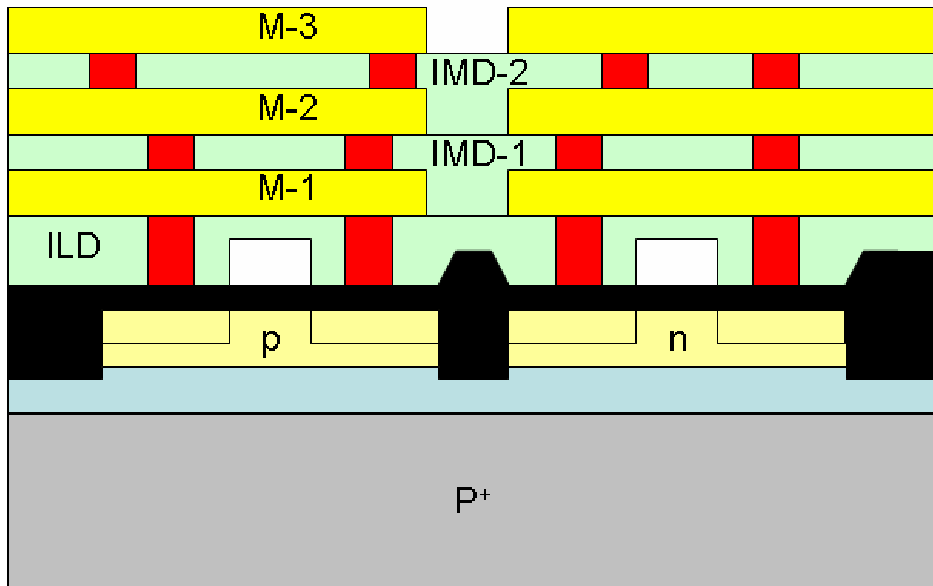


(p) After deposit and pattern the third aluminum layer

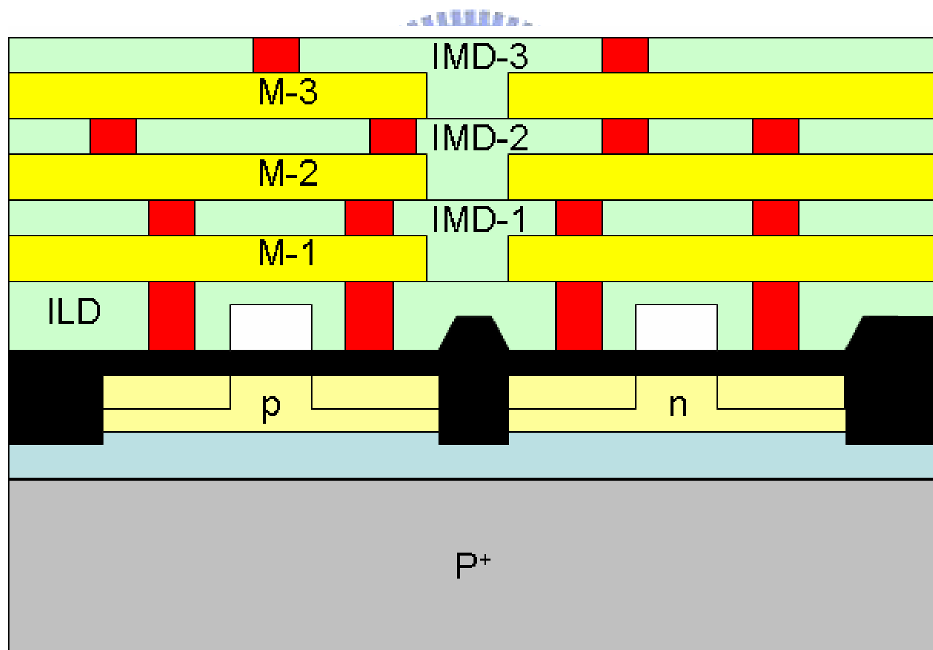


(q) After deposit the third IMD layer and the fourth tungsten layer

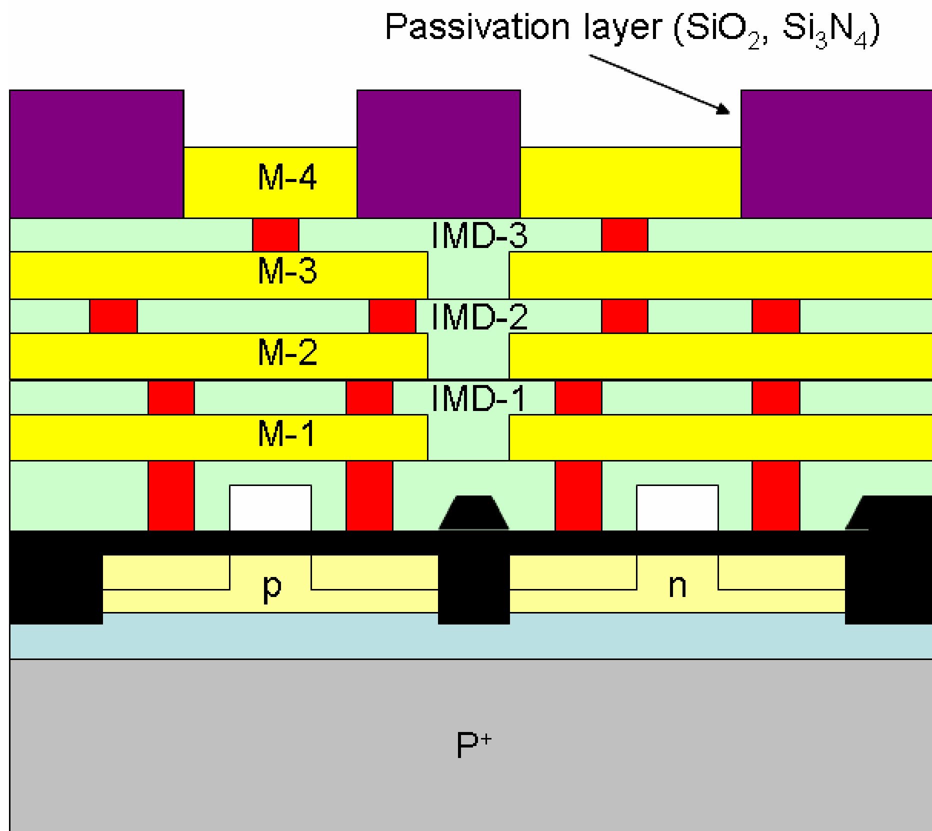


(r) After deposit and pattern the fourth aluminum layer and passivation layer.

# BIBLIOGRAPHY

[1] Y. C. Lin, The Design, Analysis, Fabrication and Application of Large Stroke Electrostatic Vertical MEMS Actuator, Ph.D. Thesis, National Chiao Tung University, 2004.

[2] T. A. Core, W. K. Tsang, and S. J. Sherman, “Fabrication Technology for an Integrated Surface-Micromachined Sensor,” *Solid State Technology*, Oct., 1993, pp. 39–47.

[3] http://www.epson.co.jp/e/newsroom/tech_news/tnl0302single.pdf

[4] L. J. Hornbeck, "Digital Light Processing and MEMS, Reflecting the Digital Display Needs of the Networked Society (Invited Plenary Paper)," *SPIE Europto Proceedings*, Vol. 2783, pp. 2–13, Besancon, France, June, 1996, pp. 12–13.

[5] A. Mohamed, H. Elsimar, and M. Ismail, “Analysis, and optimization of a CMOS vertical thermal actuator,” in *Proc. 2003 Design, Test, Integration and Packaging of MEMS/MOEMS. Symp.* , 5-7, May 2003, pp. 214–217.

[6] http://www.primetechnologywatch.org.uk/home/

[7] The PRIME Faraday Partnership, “An Introduction to MEMS,” http://www.primetechnologywatch.org.uk

[8] H. C. Nathanson, W. E. Newell, R. A. Wickstrom and J. R. Davis, “The Resonant Gate Transistor,” *IEEE Trans Electron Dev.*, Vol. 14, no. 3, pp.117–133, 1967.

[9] J. Bryzek, K. Petersen and W. McCulley, “ Micromachines on the March,” *IEEE Spectrum*, pp. 20–31, 1994.

[10]W. T. Lin, The Fabrication of Optical Communication Components Using MEMS Technology, Ph.D. Thesis, National Chiao Tung University, 2004.

[11] C. H. Mastrangelo, and C. H. Hsu, “Mechanical Stability and Adhesion of Microstructures Under Capillary Forces – Part I: Basic Theory,” *IEEE/ASME J. of Microelectromechanical Syst.*, Vol. 2, pp. 33–43, 1993.

[12] G. T. A. Kovacs, N. I. Maluf, and K. E. Petersen, “Bulk Micromachining of Silicon,” *Proceedings of the IEEE*, Vol. 86, Issue 8, Aug. 1998, pp. 1536–1551.

[13] D. B. Lee, “Anisotropic Etching of Silicon,” *J. Applied physics*, Vol.40, pp. 4569, 1969.

[14] K. Beam, “Anisotropic Etching of Silicon,” *IEEE Trans. Electron Devices*, Vol.25, pp.1185, 1978.

[15] V. Milanovic, M. Last, and K.S. J. Pister,” Laterally Actuated Torsional Micromirrors for Large Static Deflection” *IEEE Photonics tech. letters*, Vol. 15, no. 2, 2003.

[16] http://www.stsystems.com/

[17] R. A. Lawes, “Laser and electron beam based LIGA processes,” *Microengineering - the Future!* , IEE Colloquium on13 Oct 1993, pp. 7/1–7/3.

[18] F. Lärmer and A, Schilp, Patents DE 4241045, US 5501893 and EP 625285.

[19] I-H. Song and P. K. Ajmera, “Use of a photoresist sacrificial layer with SU-8 electroplating mould in MEMS fabrication,” *J. Micromech. Microeng.* Vol. 13 No 6, Nov., pp. 816–821, 2003.

[20] E. Kukharenka, M. M. Farooqui, L. Grigore, M. Kraft and N. Hollinshead, “Electroplating moulds using dry film thick negative photoresist,” *J. Micromech. Microeng.* Vol. 13, No 4, July, pp. S67–S74, 2003.

[21] http://www.aero.org/publications/helvajian/helvajian-2.html

[22] D. O. Popa, H. K. Byoung, J. T. Wen, H. E. Stephanou, G. Skidmore, and A. Geisberger, “Dynamic modeling and input shaping of thermal bimorph MEMS actuators,” in *Proc. IEEE Int. Conf. on Robotics and Automation*, (IEEE ICRA '03), 2003, Vol. 1, pp. 1470–1475.

[23] A. Tuantranont and V. M. Bright, “Micromachined thermal multimorph actuators fabricated by multi-users MEMS process,” in *Proc. IEEE Int. Conf. On Industrial Technology (IEEE ICIT '02)*, Vol. 2, pp. 941–944.

[24] S. Chowdhury, M. Ahmadi, G. A. Jullien, and W. C. Miller, “A modular MEMS electromagnetic actuator for use in a hearing instrument,” in *Proc. The 43rd IEEE Midwest Symposium on Circuits and Systems*, 2000, Vol. 1, pp. 240–243.

[25] C. H. Ji, Y. K. Kim, and B. K. Choi, “Design and fabrication of electromagnetic micromirror with bulk silicon mirror plate and aluminum spring,” in *Proc. IEEE/LEOS Optical MEMS*, 2000, pp. 97–98.

[26] J. Y. Park, Y. J. Yee, H. J. Nam, and J. U. Bu, “Micromachined RF MEMS tunable capacitors using piezoelectric actuators,” in *Proc. IEEE Microwave Symposium Digest, 2001*, Vol. 3, pp. 2111–2114.

[27] Y. Haddab, N. Chaillet, and A. Bourjault, “A microgripper using smart piezoelectric actuators,” in *Proc. IEEE Int. Conf. On Intelligent Robots and Systems (IEEE/RSJ IROS)*, 2000, Vol. 1, pp. 659–664.

[28] E. S. Hung and S. D. Senturia, “Extending the travel range of analog-tuned electrostatic actuators,” *J. Microelectromech. Syst.*, Vol. 8, Issue: 4, pp. 497–505, 1999.

[29] X. H. Mu, M. Kahrizi, L. Landsberger, “Design & fabrication of out-of-plane electrostatic actuators for optical application,” in *Proc. IEEE Canadian Conf. On Electrical and Computer Engineering (IEEE CCECE)*, 2003, Vol. 1, pp. 133–136.

[30] M. A. Rosa, S. Dimitrijev and H. B. Harrison, “Enhanced electrostatic force generation capability of angled comb finger design used in electrostatic comb-drive actuators,” *Electronics Letters*, Vol. 34, Issue: 18, pp. 1787–1788, 1998.

[31] J. Pons-Nin, A. Rodriguez and L. M. Castaner, “Voltage and pull-in time in current drive of electrostatic actuators,” *J. Microelectromech. Syst.*, Vol. 11, Issue: 3, pp. 196–205, 2002.

[32] W. Tang, T. Nguyen, and R. Howe, “Laterally driven polysilicon resonant microstructures,” *Sensors and Actuators* A, Vol. 20, pp. 25–32, 1989.

[33] W. C. Tang, Electrostatic comb drive for resonant sensor and actuator application PhD Dissertation Department of Electrical Engineering and Computer Sciences University of California, Berkeley, CA , 1990.

[33] J. W. Weigold and S. W. Pang, “Fabrication of thick Si resonators with a frontside-release etch-diffusion process,” *J. Microelectromech. Syst.*, Vol. 7, pp. 201–206, 1998.

[35] C. J. Kim, A. P. Pisano, R. S. Muller, and M. G. Lim, “Polysilicon microgrippers Tech. Digest,” *IEEE Solid-State Sensor and Actuator Workshop (Hilton Head Island, SC)*, 1990, pp. 48–51.

[36] C. H. Kim, H. M. Jeong, J. U. Jeon, and Y. K. Kim, “Silicon Micro xy-stage with a large area shuttle and no-etching holes for SPM-based data storage,” *J.*

*Microelectromech. Syst.,* Vol. 12, pp. 470–478, 2003.

[37] L. Lin, R. T. Howe, and A. P. Pisano, "Microelectromechanical filters for signal processing," *IEEE J. Microelectromech. Syst.,* Vol. 7, pp. 286–294, 1998.

[38] G. Zhou and P. Dowd 2003, "Tilted folded-beam suspension for extending the stable travel range of comb drive actuators," *J. Micromech. Microeng.,* Vol. 13, pp. 178–83, 2003.

[39] J. D. Grade, H. Jerman, and T. W. Kenny, "Design of large deflection electrostatic actuators," *J. Microelectrom. Syst.* Vol. 12, pp. 335–343, 2003.

[40] M. T. K. Hou, G. K. W. Huang, J. Y. Huang, K. M. Liao, R. Chen, and J. L. A Yeh, "Extending displacements of comb drive actuators by adding secondary comb electrodes," *J. Micromech. Microeng.,* Vol. 16, pp. 684–91, 2006.

[41] Chih-chung Chen, and Cheng-kuo Lee, "Design and modeling for comb drive actuator with enlarged static displacement," *Sensors and Actuators* A, Vol. 115, pp.530–539, 2004.

[42] H. BaLtes, O. Brand, G. F. Fedder, C. Hierold, J.G. Korvink, and O,. Yabata, Advanced Micro and Nanosystems, Vol. 2. CMOS-MEMS, WILLEY-VCH, 2005

[43] S. Ghosh and M. Bayoumi, "On integrated CMOS-MEMS system-on-chip," *IEEE-NEWCAS*, 2005, pp. 31–34.

[44] H. Baltes, O. Brand, A. Hierlemann, D. Lange, and C. Hagleitner, "CMOS MEMS – Present and Future," *IEEE MEMS*, 2002, PP. 459–466.

[45] A. Witvrouw, F. V. Steenkiste, D. Mase, L. Haspeslagh, P. V. Gerwen, P. D. Moor, S. Sedky, C. V. Hoof, A. C. D. Vries, A. Verbist, A. D. Caussemaeker, B. Parmentier, and K. Baert, "Why CMOS-integrated transducers? ," *J. Microsystem Technologies*, Vol. 6, pp.192–199, 2000.

[46] A. E. Franke, T. J. King, and R. T. Howe, "Integrated MEMS technologies," *Materials Research Society Bulletin*, April, pp. 291–295, 2001.

[47] J. Smith, S. Montague, J. Sniegowski, J. Murray, and P. McWhorter, "Embedded micromechanical devices for the monolithic integration of MEMS with CMOS," In: *Proc. IEEE IEDM ' 95*, pp. 609–612.

[48] A. A. Seshia, M. Palaniapan, T. A. Roessig, R.T. Howe, R.W. Gooch, T. R.

Schimert, and S. Montague, "A vacuum packaged surface micromachined resonant accelerometer," *J. Microelectromechan. Syst.*, Vol. 11, 784–793,2002

[49] Y. B. Gianchandani, H. Kim, M. Shinn, B. Ha, B. Lee, K. Najafi, and C. Song, "A fabrication process for integratingpolysilicon microstructures with postprocessed CMOS circuits," *J. Micromech. Microeng*., Vol. 10, pp. 380–386, 2000.

[50] J. Yasaitis, M. Judy, T. Brosnihan, P. Garone, N. Pokrovskiy, D. Sniderman, S. Limb, R. Howe, B. Boser, M. Palaniapan, X. Jiang, and S. Bhave, "A modular process for integrating thick polysilicon MEMS devices with sub-micron CMOS," In: *Proc. SPIE 2003*, 4979, 145–154.

[51] S. A. Bhave, J. I. Seeger, X. Jiang, B. E. Boser, R. T. Howe, and J. Yasaitis, "An integrated, vertical-drive, in-plane-sense microgyroscope," In: Proc. *Transducers '03*, pp. 171–174.

[52] M. W. Judy, "Evolution of integrated inertial MEMS technology," In: *Proc. Solid-State Sensor, Actuator and Microsystem Workshop*, Hilton Head Island, , pp. 27–32, 2004.

[53] A. V. Chavan, and K.D. Wise, "A monolithic fully-integrated vacuum-sealed CMOS pressure sensor," *IEEE Trans. Electron Devices*, 49, 164–169, 2002.

[54] Y. Matsumoto, and M. Esashi, "Integrated silicon capacitive accelerometer with PLL servo technique," *Sensors and Actuators A*, Vol. 39, pp. 209–217, 1993.

[55] Analog Devices, Norwood, MA, http://www.analog.com/imems/.

[56] Infineon Technologies, Munich, Germany, http://www.infineon.com/sensors/.

[57] Freescale Semiconductor (prior Motorola Semiconductor), Austin, TX, http://www.freescale.com/.

[58] T. A. Core, W. K. Tsang, and S. J. Sherman, "Fabrication technology for an integrated surface micromachined sensor," *Solid State Technol.*, pp. 39–47, 1993.

[59] S. Sugiyama, K. Kawahata, H. Funabashi, M. Takigawa, and I. Igarashi, "A 32*32 (1k)-element silicon pressure-sensor array with CMOS processing circuits," *Electron. Commun. Jpn*, Part 2 (Electronics), Vol. 75, pp.64–76, 1992.

[60] M. A. Mignardi, “From IC’ s to DMD’ s,” Texas Instrum. Tech. J., 15(3), pp. 56–63, 1998.

[61] P. F. van Kessel, L. J. Hornbeck, R. E. Meier, and M.R. Douglass, “A MEMS-based projection display,” In: *Proc. IEEE 1998*, 86, pp. 1687–1704.

[62] S. Chang, M. Chia, P. Castillo-Borelley, W. Higdon, Q. Jiang, J. Johnson, L. Obedier, M. Putty, Q. Shi, D. Sparks, and S. Zarabadi, “An electroformed CMOS integrated angular rate sensor,” *Sensors and Actuators* A, Vol. 66, 138–143, 1998.

[63] D. R. Sparks, S. R. Zarabadi, J. D. Johnson, Q. Jiang, M. Chia, O. Larsen, W. Higdon, and P. Castillo-Borelley, “A CMOS integrated surface micromachined angular rate sensor: its automotive applications,” In: *Proc. Transducers ’ 97*, pp. 851–854, 1997.

[64] D. R. Sparks, X. Huang, W. Higdon, and J. D. Johnson, “Angular rate sensor and accelerometer combined on the same micromachined CMOS chip,” *Microsyst. Technol*., Vol. 4, pp. 139–142, 1998.

[65] S. Michaelis, H.-J. Timme, M. Wycisk, and J. Binder, “Additive electroplating technology as post-CMOS process for the production of MEMS acceleration-threshold switches for transportation applications,” *J. Micromech. Microeng*., Vol. 10, pp. 120–123, 2000.

[66] M. Wycisk, T. Tonnesen, J. Binder, S. Michaelis, and H. J. Timme, “Low-cost post-CMOS integration of electroplated microstructures for inertial sensing,” *Sensors and. Actuators* A, Vol. 83, pp. 93–100, 2000.

[67] B. E. Cole, R. E. Higashi, and R. A. Wood, “Monolithic two-dimensional arrays of micromachined microstructures for infrared applications,” *Proc. IEEE 1998*, Vol. 86, pp. 1679–1686.

[68] K. Chun, and H. Kim, “Monolithic integration of the digitized pressure sensor and the micromechanical switch for the application of a pressure transponder,” *Microelectron. J*., Vol. 29, pp. 621–626, 1998.

[69] H.-J. Kress, F. Bantien, J. Marek, and M. Willmann, “Silicon pressure sensor with integrated CMOS signal-conditioning circuit and compensation of temperature coefficient,” *Sensors and Actuators* A, Vol. 25, pp. 21–26, 1996.

[70] J. G. Markle, M.L. Dunbar, H. V. Allen, R. Bornefeld, W. Schreiber-Prillwitz, and O. Stoever, “A single-chip pressure sensor,” *Sensors Mag.*, Vol. 21, pp.

27–31, 2004.

[71] V. Milanovic, E. Bowen, M. E. Zaghloul, N.H. Tea, J. S. Suehle, B. Payne, and M. Gaitan, "Micromachined convective accelerometers in standard integrated circuits technology," *Appl. Phys. Lett*., Vol. 76, pp. 508–510, 2000.

[72] F. Mayer, A. Haberli, H. Jacobs, G. Ofner, O. Paul, and H. Baltes, "Single-chip CMOS anemometer," In: *IEEE IEDM 1997*, *Technical Digest*, pp. 895–898.

[73] M. Graf, D. Barrettino, M. Zimmermann, A. Hierlemann, H. Baltes, S. Hahn, N. Barsan, U. Weimar, "CMOS monolithic metal-oxide sensor system comprising a microhotplate and associated circuitry," *IEEE Sens. J*., Vol. 4, pp. 9–16, 2004.

[74] A. D. Oliver, and K.D. Wise, "A 1024-element bulk-micromachined thermopile infrared imaging array," *Sensors and Actuators* A, Vol. 73, pp. 222–231, 1999.

[75] J. M. Bustillo, G. K. Fedder, C.T.-C. Nguyen, and R.T. Howe, "Process technology for the modular integration of CMOS and polysilicon microstructures," *Microsys. Technol.*, Vol. 1, pp. 130–141, 1994.

[76] A. E. Franke, J.M. Heck, T.-J. King, and R.T. Howe, "Polycrystalline silicon-germanium films for integrated microstructures," *J. Microelectromechan. Syst.*, Vol. 12, 160 – 171, 2003.

[77] T. Hirano, T. Furuhata, and K. J. Gabriel, "Design, fabrication, and operation of submicron gap comb drive microactuator," *J. Microelectromech. Syst.*, Vol. 1, PP. 52–59, 1992.

[78] R. Legtenberg, A. W. Groeneveld, and M. Elwenspoek, "Comb-drive actuators for large displacements," *J. Micromech. Microeng*., Vol. 6, pp. 320–329, 1999.

[79] G. Zhou and P. Dowd, "Tilted folded-beam suspension for extending the stable travel range of comb drive actuators," *J. Micromech. Microeng.,* Vol. 13, pp. 178–83, 2003.

[80] J. D. Grade, H. Jerman, and T. W. Kenny, "Design of large deflection electrostatic actuators," *J. Microelectrom. Syst.* Vol. 12, pp. 335–343, 2003.

[81] M. T. K. Hou, G. K. W. Huang, J. Y. Huang, K. M. Liao, R. Chen, and J. L. A Yeh, "Extending displacements of comb drive actuators by adding secondary

comb electrodes," *J. Micromech. Microeng.,* Vol. 16, pp. 684–91, 2006.

[82] Chih-chung Chen, and Chengkuo Lee, "Design and modeling for comb drive actuator with enlarged static displacement," *Sensors and Actuators* A, Vol. 115, pp.530–539, 2004.

[83] R. A. Lawes, "Laser and electron beam based LIGA processes," *Microengineering - the Future!* , IEE Colloquium on13 Oct 1993, pp. 7/1–7/3.

[84] F. Lärmer and A, Schilp, Patents DE 4241045, US 5501893 and EP 625285.

[85] I-H. Song and P. K. Ajmera, "Use of a photoresist sacrificial layer with SU-8 electroplating mould in MEMS fabrication," *J. Micromech. Microeng.* 13 No 6, Nov., pp. 816–821, 2003.

[86] E. Kukharenka, M. M. Farooqui, L. Grigore, M. Kraft and N. Hollinshead, "Electroplating moulds using dry film thick negative photoresist," *J. Micromech. Microeng.* 13**,** No 4, July, pp. S67–S74, 2003.

[87] E. T. Carlen, K. H. Heng, S. Bakshi, A. Pareek, and C. H. Mastrangelo, "High-aspect ratio vertical. comb-drive actuator with small self-aligned finger gaps," *J. Microelectromech. Syst*., Vol. 14, pp. 1144–1155, 2005.

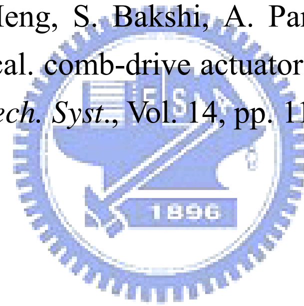

# BIOGRAPHY

## 學歷：

| | | |
|---|---|---|
| 博士 | 交通大學 電機與控制工程學系 | 2001.9 ~ 2007.10 |
| 碩士 | 義守大學 電機工程研究所 | 1999.9 ~ 2001.7 |
| 學士 | 逢甲大學 自動控制工程學系 | 1994.9 ~ 1999.7 |
| 高中 | 台南第一高級中學 | 1989.9 ~ 1992.7 |
| 國中 | 台南縣新市國中 | 1986.9 ~ 1989.7 |
| 國小 | 台南縣新市國小 | 1980.9 ~ 1986.7 |

## 經歷：

**（1）研究助理：**

經濟部科專計畫：微光機電系統晶片研發計畫--分項計畫一：微光機電系統

2002.12～2005.11

國科會整合型計畫：以生理訊號為基礎之人機介面系統--子計畫六(1/3)：應用於生理訊號量測系統之多波段波長可調變微機電晶片研究

2004.08～2005.07

# PUBLICATION

Journal Papers

1. Jin-Chern Chiou, Chin-Fu Kuo, and Yung-Jiun Lin, “A Micromirror with Large Static Rotation and Vertical Actuation” *IEEE Journal of Selected Topics in Quantum Electronics* , Vol. 13, pp. 297-303, 2007..
2. Jin-Chern Chiou and Chin-Fu Kuo, “Development of Vertical Electrostatic Comb-Drive Actuator Using Magnified Cascade Configuration,” *Japan Journal of Applied Physics* (accept).
3. Jin-Chern Chiou, Chin-Fu Kuo, and Yung-Jiun Lin, “Extending Traveling Range with a Cascade Electrostatic Comb-Drive Actuator,” *Journal of Micromechanics. Microengineering* (revised).

Conference Papers

1. J. C. Chiou, C. F. Kuo, and Y. C. Lin, “A Tilting Micromirror with Well-Controlled Digital Angle Through Constrained Lever Structure”, *SPIE Photonics Europe (MEMS, MOEMS, and Micromachining) 2004*.
2. C. F. Kuo, J. C. Chiou, and W. T. Lin, “Self-Aligned Multi-Layers SOI Process for MEMS Applications,” *Optics and Photonics Taiwan 2004.*
3. Jin-Chern Chiou, Chin-Fu Kuo, and Yung-Jiun Lin, “The Implementation of a Novel Magnified Cascade Configuration Using A Vertical Electrostatic Actuator”, *IEEE Conference on Nanotechnology 2006*.
4. Jin-Chern Chiou, Chin-Fu Kuo, and Yung-Jiun Lin, “A Micromirror with Large Static Rotation and Piston Actuation”, *IEEE Optical MEMS 2006*.
5. J. C. Chiou, C. F. Kuo, Y. J. Lin, C.W. Chang, K. C. Hou, “Development of Novel Cascade Structure for Improving Stroke of Electrostatic Comb-Drive Actuator,” *IEEE MEMS 2008*.